



# Magnetoelastic instabilities in soft laminates with ferromagnetic hyperelastic phases

Parag Pathak<sup>a</sup>, Nitesh Arora<sup>a</sup>, Stephan Rudykh<sup>a,b,\*</sup>

<sup>a</sup> Department of Mechanical Engineering, University of Wisconsin – Madison, Madison, WI 53706, United States

<sup>b</sup> School of Mathematical & Statistical Sciences, National University of Ireland Galway, University Road, Galway, Ireland

## ARTICLE INFO

### Keywords:

Magnetoactive elastomers  
Microstructure  
Magnetostriction  
Instabilities  
Finite deformation  
Laminates

## ABSTRACT

We investigate the microscopic and macroscopic instabilities developing in magnetoactive elastomer (MAE) composites undergoing large deformations in the presence of an external magnetic field. In particular, we consider the MAEs with bi-phasic layered microstructure, with phases exhibiting ferromagnetic behavior. We derive an explicit expression for the magnetic field-induced deformation of MAEs with hyperelastic phases. To perform the magnetoelastic instability analysis, we employ the small-amplitude perturbations superimposed on finite deformations in the presence of the magnetic field. We examine the interplay between the macroscopic and microscopic instabilities. We find that the layered MAEs can develop microscopic instability with *antisymmetric* buckling modes, in addition to the classical *symmetric* mode. Notably, the antisymmetric microscopic instability mode does not appear in a purely mechanical scenario (when a magnetic field is absent). Furthermore, our analysis reveals that the wavelength of buckling patterns is highly tunable by the applied magnetic field, and by the properties and volume fractions of the phases. Our findings provide the information for designing materials with reconfigurable microstructures. This material ability can be used to actively tune the behavior of materials by a remotely applied magnetic field. The results can be utilized in designing tunable acoustic metamaterials, soft actuators, sensors, and shape morphing devices.

## 1. Introduction

Magnetoactive elastomers (MAEs) belong to a class of soft active materials that respond to remotely applied magnetic field. The application of magnetic field results in the modification of mechanical behavior and deformation (also referred to as *magnetostriction*) of these active materials. Thanks to their simple, remote, and reversible principle of operation, MAEs can provide the material platform for applications such as variable-stiffness devices [1,2], tunable vibration absorbers [3,4], damping devices [5,6], sensors [7,8], noise barriers [9,10], remotely controlled actuators [11–14], biomedicine [15], and soft robotics [16,17] among many others.

In principle, MAEs are composite materials consisting of magnetizable particles (for example, carbonyl iron, nickel, or Terfenol-D) embedded in an elastomeric matrix material (such as silicone rubber, polyurethane) [18]. The magnetizable particles (from micro- to nano-size) are added into the matrix material in its liquid state. Upon polymerization, the MAEs with randomly distributed magnetizable particles are produced. Curing in the presence of a magnetic field,

however, results in the alignment of magnetizable particles into chain-like structures (for a detailed description of the MAE synthesis, interested readers are referred to the review article by Bastola and Hossain [19]).

There is a significant body of studies concerning the magneto-mechanical characterization of MAEs with different microstructures “random and chain-like” are present in the literature. Jolly et al. [18] and Danas et al. [20] studied the shear response of chain-structured MAEs, showing, for example, that the effective shear modulus increases in the presence of a magnetic field. The effective moduli of MAEs are also reported to be increased by the applied magnetic field under uniaxial compression [21] and tensile tests [22]. The magnetostriction of MAEs with randomly distributed magnetizable particles under a very high magnetic field is analyzed by Bednarek [23]. Ginder et al. [2] and Guan et al. [24] determined the magnetostriction of random and chain-structured MAEs. The effect of particle rotation on the effective magnetization of MAEs is investigated by Lanotte et al. [25]. Moreno et al. [26] provided a comprehensive experimental characterization of MAEs with a special focus on the material response under various strain

\* Corresponding author.

E-mail address: [rudykh@wisc.edu](mailto:rudykh@wisc.edu) (S. Rudykh).

<https://doi.org/10.1016/j.ijmecsci.2021.106862>

Received 8 August 2021; Received in revised form 1 October 2021; Accepted 2 October 2021

Available online 11 October 2021

0020-7403/© 2021 The Author(s). Published by Elsevier Ltd. This is an open access article under the CC BY license (<http://creativecommons.org/licenses/by/4.0/>).

rates. Dargahi et al. [27] performed the dynamic characterization of MAEs subjected to a wide range of excitation frequencies and magnetic flux densities. In these studies, the magnetizable particles are effectively rigid as compared to the elastomer matrix. The magneto-mechanical coupling observed in these MAEs is therefore majorly governed by the two underlying mechanisms, namely, magnetic torques and magnetic interaction between the particles.

The pioneering works of Brown [28], Maugin and Eringen [29], Tiersten [30], Toupin [31], Truesdell and Toupin [32] laid the foundation for the theory of magnetoelastic (and mathematically analogous electroelastic) behavior of continuum, which has been reformulated and further developed [33–35]. In parallel, a number of microstructural-based magneto-elastic constitutive models are also developed, for example the lattice model [18,36,37]. Additionally, significant efforts have been made to implement the non-linear magnetoelastic framework into numerical schemes [38–40]. Castañeda and Galipeau [41] proposed an analytical approach to estimate the effective behavior of MAEs with the random distribution of magnetoactive particles. In particular, they developed a finite strain nonlinear homogenization framework to determine the total magnetoelastic stress in MAEs under the combined mechanical and magnetic loading. By employing this framework, Galipeau and Castañeda [42] studied the effects of randomly distributed magnetizable particle shape, distribution, and concentration on the effective properties of MAEs. Moreover, Galipeau et al. [43] investigated the behavior of MAEs with periodic arrangements of circular and elliptical fibers, showing that by tailoring the periodic microstructure of MAEs, their magneto-mechanical behavior could be highly tuned. We note that these systems share some similarities with their mathematically analogous dielectric elastomer composites [44–46].

While the heterogeneity provides access to the tailored and enhanced coupled behavior, it is also a source for the development of microstructural instabilities. The instability phenomenon historically has been considered as a failure mode, which is to be predicted and avoided. This motivated the investigation of instabilities in composites subjected to purely mechanical loading [47–56]. Recently, the elastic instability phenomenon has been embraced to design materials with unusual properties and switchable functionalities [57,58]. Examples include instability-induced elastic wave band gaps [59,60], auxetic behavior [61–63], and photonic switches [64]. The possibility of controlling the instability development via magnetic field can provide the opportunity to activate these functionalities remotely.

Extending the instability analysis for the coupled magneto-mechanical case, Ottenio et al. [65] studied the onset of magneto-mechanical instabilities in isotropic MAEs with a focus on surface instabilities of a homogeneous magnetoactive half-space. Kankanala and Triantafyllidis [66] investigated the failure modes of a rectangular MAE subjected to plane-strain loading conditions in the presence of a magnetic field. Rudykh and Bertoldi [67] analyzed the onset of macroscopic instabilities in anisotropic MAEs by deriving the exact solution for MAEs with layered microstructure. Danas and Triantafyllidis [68] studied the finite-wavelength instability modes occurring in an MAE substrate/layer system under a transverse magnetic field. Recently, Goshkoderia and Rudykh [69] employed a numerical finite element-based code to investigate macroscopic instabilities in MAEs with circular and elliptical inclusions. Very recently, Goshkoderia et al. [70] experimentally illustrated that the instability pattern can be tailored by the application of magnetic field in particulate magneto-active composites.

Motivated by recent experimental studies showing the tunability of finite-wavelength instabilities via magnetic field [70,71], in this work, we study the onset of microscopic instabilities and associated buckling patterns in MAEs. In particular, we consider the MAEs with bi-phasic layered microstructure exhibiting ferromagnetic behavior. To investigate the onset of instabilities, we consider the small-amplitude perturbations superimposed on finite deformations in the presence of magnetic

field to perform the microscopic instability analysis. Moreover, we analyze the limit corresponding to the long-wave or macroscopic instability. We examine the influences of the applied magnetic field and material parameters on MAE's stability. Additionally, we study the magnetostriction of layered MAEs and derive an explicit expression for the induced stretch as a function of the applied magnetic field, mechanical and magnetic properties of layers, and their volume fractions.

This paper is structured as follows: Section 2 presents the theoretical background on magneto-elastostatics and incremental analysis together with the constitutive laws for magnetically linear and ferromagnetic behavior. Section 3 is concerned with the analysis of the magneto-deformation and determination of the microscopic and macroscopic instabilities in layered MAEs. Section 4 illustrates the results with examples of magnetostriction and magnetoelastic instabilities in MAEs with various morphologies and material properties. Section 5 concludes the paper with a summary and a discussion.

## 2. Theoretical background

### 2.1. Magneto-elastostatics

Consider a magnetoelastic deformable body that occupies a region  $\mathfrak{B}_0$  in the undeformed configuration. Under the action of a combination of mechanical loading and magnetic field, the body deforms into the current configuration  $\mathfrak{B}$ . The deformation is described by the function  $\mathbf{x}$  that maps the reference point  $\mathbf{X}$  in  $\mathfrak{B}_0$  to its deformed position  $\mathbf{x} = \mathbf{x}(\mathbf{X})$  in  $\mathfrak{B}$ . The deformation gradient is thus defined as  $\mathbf{F} = \partial\mathbf{x}/\partial\mathbf{X}$  with its determinant  $J \equiv \det\mathbf{F} > 0$ .

In this work, we consider quasi-static deformation in the absence of an electric field, electrical charges, or electrical currents within the material. Consequently, the magnetic induction  $\mathbf{B}$  and magnetic intensity  $\mathbf{H}$  (in the current configuration) satisfy the following field equations

$$\text{div}\mathbf{B} = 0 \quad \text{and} \quad \text{curl}\mathbf{H} = \mathbf{0}, \quad (1)$$

where the div and curl are the differential operators defined with respect to  $\mathbf{x}$ . In the Lagrangian form, Eq. (1) can be written as [33]

$$\text{Div}\mathbf{B}^0 = 0 \quad \text{and} \quad \text{Curl}\mathbf{H}^0 = \mathbf{0}, \quad (2)$$

where the Div and Curl operators are defined with respect to  $\mathbf{X}$ ,  $\mathbf{B}^0 = \mathbf{J}\mathbf{F}^{-1}\mathbf{B}$  and  $\mathbf{H}^0 = \mathbf{F}^T\mathbf{H}$  are the Lagrangian counterparts of the magnetic fields. Moreover, in a heterogeneous body, magnetic fields satisfy the jump conditions across the interface

$$[[\mathbf{B}]] \cdot \mathbf{N} = 0 \quad \text{and} \quad [[\mathbf{H}]] \times \mathbf{N} = \mathbf{0}, \quad (3)$$

or alternatively,

$$[[\mathbf{B}^0]] \cdot \mathbf{N}^0 = 0 \quad \text{and} \quad [[\mathbf{H}^0]] \times \mathbf{N}^0 = \mathbf{0}, \quad (4)$$

where  $\mathbf{N}$  and  $\mathbf{N}^0$  denote the normal to the interface in the deformed and reference configurations, respectively. The jump operator  $[[\bullet]] \equiv (\bullet)^+ - (\bullet)^-$  is defined such that  $\mathbf{N}$  and  $\mathbf{N}^0$  are pointing towards phase  $(\bullet)^-$ . The magnetization is customarily defined as

$$\mathbf{M} = \frac{\mathbf{B}}{\mu_0} - \mathbf{H}, \quad (5)$$

where  $\mu_0$  is the vacuum magnetic permeability.

Following the works of Brown [28], Coleman and Noll [72], Kovetz [73], the magnetization is constitutively defined in terms of free-energy function  $\phi(\mathbf{F}, \mathbf{B})$  as

$$\mathbf{M} = -\rho \frac{\partial\phi}{\partial\mathbf{B}}, \quad (6)$$

where  $\rho$  is the material density in the current configuration. The *total*

Cauchy stress  $\sigma$  is given by

$$\sigma = \rho \frac{\partial \phi}{\partial \mathbf{F}} \mathbf{F}^T - \frac{1}{2\mu_0} (\mathbf{B} \cdot \mathbf{B}) \mathbf{I} + \mathbf{H} \otimes \mathbf{B} + (\mathbf{M} \cdot \mathbf{B}) \mathbf{I}. \quad (7)$$

In terms of these relations, the energy-density function  $\phi$  fully characterizes the behavior of magneto-active elastomers. Note that in the absence of material (or vacuum), the stress tensor (7) is still non-zero and depends on the magnetic field. The corresponding stress tensor is also referred to as Maxwell stress. The free energy in Lagrangian form is defined as  $\Phi(\mathbf{F}, \mathbf{B}^0) = \phi(\mathbf{F}, J^{-1} \mathbf{F} \mathbf{B}^0)$ . In terms of  $\Phi$ , a Lagrangian amended energy function can be constructed as [33]

$$W(\mathbf{F}, \mathbf{B}^0) = \rho_0 \Phi(\mathbf{F}, \mathbf{B}^0) + \frac{\mathbf{F} \mathbf{B}^0 \cdot \mathbf{F} \mathbf{B}^0}{2\mu_0 J}, \quad (8)$$

where  $\rho_0 = \rho J$  is the material density in the reference configuration. Then, the corresponding Lagrangian variables are given by

$$\mathbf{H}^0 = \frac{\partial W}{\partial \mathbf{B}^0} \quad \text{and} \quad \mathbf{P} = \frac{\partial W}{\partial \mathbf{F}}, \quad (9)$$

where  $\mathbf{P}$  is the 1st Piola Kirchhoff stress tensor. Eqs. (7)–(9) hold true for compressible hyperelastic materials. For incompressible materials ( $J = 1$ ), however, the total Cauchy stress tensor is

$$\sigma = \frac{\partial W}{\partial \mathbf{F}} \mathbf{F}^T - p \mathbf{I}, \quad (10)$$

where  $p$  is the Lagrange multiplier associated with the incompressibility constraint.

In the absence of body forces, the total Cauchy and 1st Piola-Kirchhoff stress tensors satisfy the equilibrium conditions

$$\text{div} \sigma = \mathbf{0} \quad \text{and} \quad \text{Div} \mathbf{P} = \mathbf{0}. \quad (11)$$

The corresponding jump conditions at the interface are

$$[[\sigma]] \cdot \mathbf{N} = 0 \quad \text{and} \quad [[\mathbf{P}]] \cdot \mathbf{N} = 0. \quad (12)$$

## 2.2. Incremental equations

Here, following the approach commonly used to study instabilities [65,67,69,74,75], we define the governing equations for the incremental deformation superimposed on finite deformation in the presence of a magnetic field. The incremental governing equations are

$$\text{Div} \dot{\mathbf{P}} = \mathbf{0}, \quad \text{Div} \dot{\mathbf{B}} = 0 \quad \text{and} \quad \text{Curl} \dot{\mathbf{H}} = \mathbf{0}, \quad (13)$$

where  $\dot{\mathbf{P}}$ ,  $\dot{\mathbf{B}}$ , and  $\dot{\mathbf{H}}$  are the incremental changes in  $\mathbf{P}$ ,  $\mathbf{B}^0$ , and  $\mathbf{H}^0$ , respectively. Under the assumption that the incremental quantities are sufficiently small, the linearized constitutive relations can be expressed using the Einstein summation notation as

$$\dot{P}_{ij} = \mathcal{A}_{ijkl}^0 \dot{F}_{kl} + \mathcal{M}_{ijk}^0 \dot{B}_k^0, \quad \text{and} \quad \dot{H}_i = \mathcal{M}_{ikl}^0 \dot{F}_{kl} + \mathcal{H}_{ik}^0 \dot{B}_k^0, \quad (14)$$

where

$$\mathcal{A}_{ijkl}^0 = \frac{\partial^2 W}{\partial F_{ij} \partial F_{kl}}, \quad \mathcal{M}_{ijk}^0 = \frac{\partial^2 W}{\partial F_{ij} \partial B_k^0}, \quad \text{and} \quad \mathcal{H}_{ik}^0 = \frac{\partial^2 W}{\partial B_i^0 \partial B_k^0}. \quad (15)$$

For an incompressible material, Eq. (14)<sub>1</sub> modifies to

$$\dot{P}_{ij} = \mathcal{A}_{ijkl}^0 \dot{F}_{kl} + \mathcal{M}_{ijk}^0 \dot{B}_k^0 - \dot{p} F_{ij}^{-T} + p F_{jk}^{-1} \dot{F}_{kl} F_{li}, \quad (16)$$

where  $\dot{p}$  is the incremental change in  $p$ .

In the current configuration, the magnetoelastic moduli are defined as

$$\mathcal{A}_{ijkl} = J^{-1} F_{ja} F_{ib} \mathcal{A}_{ikab}^0, \quad \mathcal{M}_{ijk} = F_{ja} F_{kb} \mathcal{M}_{iab}^0, \quad \text{and} \quad \mathcal{H}_{ij} = J F_{ia}^{-1} F_{jb}^{-1} \mathcal{H}_{ab}^0, \quad (17)$$

and they possess the following symmetries

$$\mathcal{A}_{ijkl} = \mathcal{A}_{klij}, \quad \mathcal{M}_{ijk} = \mathcal{M}_{kij}, \quad \text{and} \quad \mathcal{H}_{ij} = \mathcal{H}_{ji}. \quad (18)$$

The updated incremental governing equations take the form

$$\text{div} \dot{\sigma} = \mathbf{0}, \quad \text{div} \dot{\mathbf{B}} = 0, \quad \text{and} \quad \text{curl} \dot{\mathbf{H}} = \mathbf{0}, \quad (19)$$

where  $\dot{\sigma}$ ,  $\dot{\mathbf{B}}$ , and  $\dot{\mathbf{H}}$  are the “push-forward” counterparts of  $\dot{\mathbf{P}}$ ,  $\dot{\mathbf{B}}^0$ , and  $\dot{\mathbf{H}}^0$ , respectively. These incremental changes are related as

$$\dot{\sigma} = J^{-1} \mathbf{F}^T \dot{\mathbf{P}}, \quad \dot{\mathbf{B}} = J^{-1} \mathbf{F} \dot{\mathbf{B}}^0, \quad \text{and} \quad \dot{\mathbf{H}} = \mathbf{F}^{-T} \dot{\mathbf{H}}^0. \quad (20)$$

We define the incremental displacement  $\mathbf{v} = \dot{\mathbf{x}}$  with  $\dot{\mathbf{F}} = (\text{grad} \mathbf{v}) \mathbf{F}$ . Substituting Eqs. (14), (16), and (17) into Eq. (20), we obtain

$$\dot{\sigma}_{ij} = \mathcal{A}_{ijkl} \frac{\partial v_k}{\partial x_l} + \mathcal{M}_{ijk} \dot{B}_k - \dot{p} \delta_{ij} + p \frac{\partial v_j}{\partial x_i}, \quad \text{and} \quad \dot{H}_i = \mathcal{M}_{ijk} \frac{\partial v_j}{\partial x_k} + \mathcal{H}_{ik} \dot{B}_k. \quad (21)$$

Upon substitution of Eq. (21) into Eqs. (19)<sub>1</sub> and (19)<sub>3</sub>, we obtain

$$\mathcal{A}_{ijkl} \frac{\partial^2 v_k}{\partial x_j \partial x_l} + \mathcal{M}_{ijk} \frac{\partial \dot{B}_k}{\partial x_j} - \frac{\partial \dot{p}}{\partial x_i} = 0 \quad \text{and} \quad \epsilon_{isp} \left( \mathcal{M}_{ijk} \frac{\partial^2 v_j}{\partial x_k \partial x_p} + \mathcal{H}_{ij} \frac{\partial \dot{B}_j}{\partial x_p} \right) = 0, \quad (22)$$

where  $\epsilon_{isp}$  is the Levi-Civita permutation tensor.

## 2.3. Magnetic energy functions

In this work, we assume the magnetoactive elastomers to be magnetically soft, so that the hysteresis effects can be neglected. Moreover, we consider the magnetic particles to be isotropic and superparamagnetic, i.e., demagnetization effects are neglected. On the basis of whether the materials show saturation effects, they can be constitutively defined either by linear or ferromagnetic material models.

### 2.3.1. Linear magnetic materials

Linear magnetic materials show a linear dependence of magnetization on the magnetic induction  $\mathbf{B}$ , namely,

$$\mu_0 \mathbf{M} = \chi \mathbf{B}, \quad (23)$$

where  $\chi$  is the magnetic susceptibility.<sup>1</sup> Alternatively, the constitutive relation can be written as

$$\mathbf{B} = \mu \mathbf{H}, \quad (24)$$

where  $\mu = \mu_0 / (1 - \chi)$  is the magnetic permeability. The corresponding magnetic energy is

$$\rho \phi_m(\mathbf{B}) = -\frac{1}{2\mu_0} \mathbf{B} \cdot \chi \mathbf{B}. \quad (25)$$

### 2.3.2. Ferromagnetic materials

For ferromagnetic materials, the magnetization reaches a saturation state at sufficiently high magnetic fields, beyond which there is no further increase in magnetization. Assuming the soft ferromagnetic behavior and magnetic particles being large compared to the typical domain size, the material behavior can be idealized as having a single-valued constitutive behavior. Although other models can be used, we use the isotropic Langevin model to define the ferromagnetic behavior in the forthcoming analysis. For this model, the magnetization is defined by the following relation

<sup>1</sup> In this work, we use the magnetic susceptibility,  $\chi$ , defined via magnetic induction as  $\mu_0 \mathbf{M} = \chi \mathbf{B}$ . Note the alternative definition of magnetic susceptibility in terms of magnetic intensity is  $\mathbf{M} = \chi_H \mathbf{H}$ . These susceptibilities are related as  $\chi_H = \chi / (1 - \chi)$ .

$$\mathbf{M}(\mathbf{B}) = \frac{m_s}{B} \left[ \coth\left(\frac{3\chi B}{\mu_0 m_s}\right) - \frac{\mu_0 m_s}{3\chi B} \right] \mathbf{B}, \quad (26)$$

where  $m_s$  is the saturation magnetization and  $B$  is the magnitude of the magnetic induction vector  $\mathbf{B}$ , i.e.,  $B = |\mathbf{B}|$ . Alternatively, the constitutive relation can also be expressed as

$$\mathbf{B} = \mu(B)\mathbf{H}, \quad (27)$$

where

$$\mu(B) = \mu_0 \left( 1 - \frac{\mu_0 m_s}{B} \left[ \coth\left(\frac{3\chi B}{\mu_0 m_s}\right) - \frac{\mu_0 m_s}{3\chi B} \right] \right)^{-1}. \quad (28)$$

The corresponding magnetic energy is

$$\rho\phi_m(B) = -\frac{\mu_0 m_s^2}{3\chi} \left[ \ln\left(\sinh\left[\frac{3\chi B}{\mu_0 m_s}\right]\right) - \ln\left(\frac{3\chi B}{\mu_0 m_s}\right) \right]. \quad (29)$$

Fig. 1 a illustrates the magnetic  $B-H$  dependence for linear and ferromagnetic materials. Here, we plot the magnitude of magnetic intensity  $H$  as the function of  $B$ , for materials with initial susceptibility  $\chi = 0.9$ . The black solid curve represents the behavior of the linear magnetic material. The non-solid curves show the response of ferromagnetic materials with magnetic saturation values:  $\mu_0 m_s = 2$  T (red dash-dotted curve),  $\mu_0 m_s = 5$  T (blue dotted curve), and  $\mu_0 m_s = 10$  T (green dashed curve). As expected, the  $B-H$  curve for linear magnetic material shows a linear response. However, for ferromagnetic materials, the dependence is nonlinear, specifically at small magnetic fields. However, once the saturation limit of magnetization is achieved at a relatively high magnetic field, they show the linear relation in  $H$  and  $B$ .

Fig. 1 b shows the normalized magnitude of magnetization  $M/m_s$  as the function of normalized magnetic induction  $B/(\mu_0 m_s)$ . The solid curves represent the response of the ferromagnetic materials, whereas the dash-dotted curves correspond to the linear magnetic materials. We consider the materials with three initial susceptibilities:  $\chi = 0.9$  (black curves),  $\chi = 0.7$  (green curves), and  $\chi = 0.5$  (red curves). As expected, the linear magnetic materials show the linear dependence of magnetization on magnetic induction, with slopes proportional to their corresponding magnetic susceptibilities  $\chi$ . Ferromagnetic materials also show the linear response, however, only at small magnetic fields. At relatively high magnetic induction magnitudes, the magnetization in these materials approaches the saturation values,  $M/m_s \rightarrow 1$  (see the solid curves). In ferromagnetic materials with higher initial susceptibilities, the saturation magnetization values are achieved at comparatively smaller magnetic induction magnitudes.

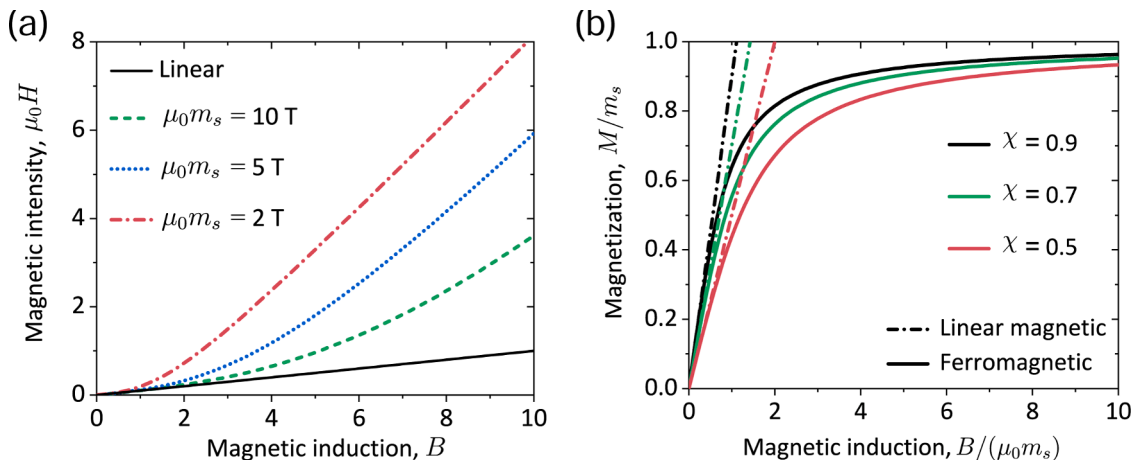


Fig. 1. The dependence of magnetic intensity magnitude  $H$  (a) and magnetization  $M$  (b) on the magnetic induction magnitude  $B$ ; initial susceptibility is  $\chi = 0.9$  in (a).

### 3. Analysis and Results

We examine incompressible magnetoactive elastomers with bilayer microstructure (schematically shown in Fig. 2) having lamination direction  $\mathbf{L}$ . The volume fraction of the matrix phase is  $c^{(m)}$ , and that of the stiff layer is  $c^{(f)} = 1 - c^{(m)}$ . Here and thereafter, we denote the parameters and fields corresponding to the matrix and stiff layers as  $(\bullet)^{(m)}$  and  $(\bullet)^{(f)}$ , respectively. The average deformation gradient  $\bar{\mathbf{F}}$  and magnetic induction  $\bar{\mathbf{B}}$  are defined as

$$\bar{\mathbf{F}} = c^{(m)}\mathbf{F}^{(m)} + c^{(f)}\mathbf{F}^{(f)} \quad \text{and} \quad \bar{\mathbf{B}} = c^{(m)}\mathbf{B}^{(m)} + c^{(f)}\mathbf{B}^{(f)}. \quad (30)$$

In this work, we investigate the magneto-mechanical loading defined as

$$\bar{\mathbf{F}} = \lambda \mathbf{e}_1 \otimes \mathbf{e}_1 + \lambda_2 \mathbf{e}_2 \otimes \mathbf{e}_2 + \mathbf{e}_3 \otimes \mathbf{e}_3 \quad \text{and} \quad \bar{\mathbf{B}} = B \mathbf{e}_2, \quad (31)$$

where  $\lambda$  is the stretch along the direction of layers, and  $\lambda_2 = \lambda^{-1}$  for incompressible MAEs. Note that we consider an idealization of the periodic microstructure unit cells (schematically shown in Fig. 2b) situated far from the specimen boundaries. Under the assumed separation of length scales, the mechanical and magnetic fields can be considered to be homogeneous in each layer of the laminate and are determined by the appropriate jump conditions.

The displacement continuity condition at the layer interface implies

$$(\mathbf{F}^{(m)} - \mathbf{F}^{(f)}) \cdot \mathbf{s} = \mathbf{0} \quad (32)$$

where  $\mathbf{s}$  is a unit vector perpendicular to the lamination direction  $\mathbf{L}$ . Using Eq. (32), for the deformation gradient  $\bar{\mathbf{F}}$  (31)<sub>1</sub> with incompressible phases, we can write

$$\mathbf{F}^{(m)} = \mathbf{F}^{(f)} = \lambda \mathbf{e}_1 \otimes \mathbf{e}_1 + \lambda^{-1} \mathbf{e}_2 \otimes \mathbf{e}_2 + \mathbf{e}_3 \otimes \mathbf{e}_3. \quad (33)$$

In the deformed configuration, the thicknesses of the matrix and stiff layers are  $L^{(m)} = c^{(m)}L$  and  $L^{(f)} = c^{(f)}L$ , respectively, where  $L$  is the period of the layered material in the current state. Moreover, using the magnetic induction jump condition (3) at the interface for the current magnetic loading (31)<sub>2</sub>, we obtain

$$\mathbf{B}^{(f)} = \mathbf{B}^{(m)} = B \mathbf{e}_2. \quad (34)$$

We consider the laminates with the isotropic layers, with each layer  $(r) \in \{m, f\}$  defined by the following amended energy function

$$W^{(r)} = W_e^{(r)} + W_m^{(r)}, \quad (35)$$

where  $W_e^{(r)}$  is the elastic part and  $W_m^{(r)}$  is the magnetic part. Although the analysis presented here is general, we consider the elastic part of both

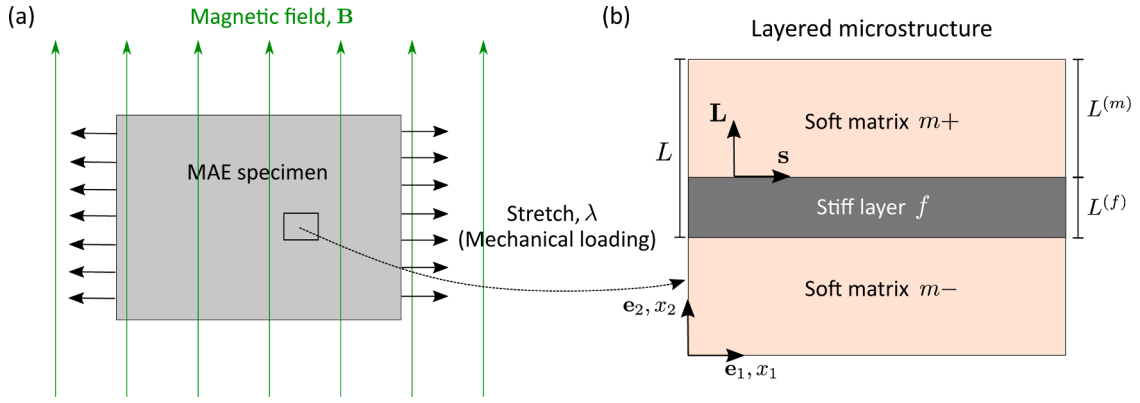


Fig. 2. Magnetoactive elastomer (MAE) specimen is placed in the presence of an external magnetic field (a). The MAE has layered microstructure (b).

phases to adopt the neoHookean material model for simplicity. The corresponding energy function is

$$W_e^{(r)} = \frac{G^{(r)}}{2} (I_1 - 3), \quad (36)$$

where  $G^{(r)}$  is the shear modulus of the phase  $(r)$  and  $I_1^{(r)} = \text{tr} \mathbf{C}^{(r)}$ ,  $\mathbf{C}^{(r)} = \mathbf{F}^{(r)\top} \mathbf{F}^{(r)}$  is the right Cauchy-Green deformation tensor, and  $\mathbf{F}^{(r)}$  is the deformation gradient. The magnetic part of the amended energy function  $W_m^{(r)}$  for each layer is defined as

$$W_m^{(r)} = \rho^{(r)} \phi_m^{(r)} + \frac{1}{2\mu_0} \mathbf{B} \cdot \mathbf{B}, \quad (37)$$

where the term  $\rho^{(r)} \phi_m^{(r)}$  can be defined either using the expression (25) or (29), according to the magnetic behavior of the layer;  $\mathbf{B}^{(r)}$  denotes the magnetic induction vector. Note that the second term,  $\mathbf{B}^{(r)} \cdot \mathbf{B}^{(r)} / (2\mu_0)$ , is independent of material constants; therefore, the magnetic energy is non-zero in the free space or in a non-magnetic material. The non-zero components of the corresponding magnetoelastic moduli tensors  $\mathcal{A}_{ijkl}$ ,  $\mathcal{M}_{ijk}$ , and  $\mathcal{N}_{ij}$  for each phase are provided in Appendix A, separately for both types of magnetic behaviors – linear and ferromagnetic.

### 3.1. Magnetostriction

Here, we evaluate the deformation of the magnetoactive laminates with the application of magnetic field (31)<sub>2</sub>, without any mechanical traction. In particular, we study the homogenized response of the periodic unit cell shown in Fig. 2b. Using Eq. (10), the stress field inside an incompressible layer  $(r)$ , with the amended energy function given by Eqs. (35)–(37) can be written as

$$\boldsymbol{\sigma}^{(r)} = G^{(r)} \mathbf{F} \mathbf{F}^T + \frac{1}{\mu^{(r)}} \bar{\mathbf{B}} \otimes \bar{\mathbf{B}} - p^{(r)} \mathbf{I}, \quad (38)$$

where the magnetic permeability  $\mu^{(r)}$  can either be constant or a function of  $B$  (28) depending on the choice of the energy function.

The stress field jump condition across the interface  $\mathbf{L} = \mathbf{e}_2$  yields  $\sigma_{22}^{(f)} = \sigma_{22}^{(m)}$ . We assume that the finite MAE specimen (Fig. 2a) is surrounded by a vacuum. Using the mechanical traction-free boundary conditions and the stress field jump condition, we obtain

$$c^{(m)} \boldsymbol{\sigma}^{(m)} + c^{(f)} \boldsymbol{\sigma}^{(f)} = \boldsymbol{\sigma}_m^*, \quad (39)$$

where  $\boldsymbol{\sigma}_m^*$  is the Maxwell stress tensor defined as

$$\boldsymbol{\sigma}_m^* = \frac{1}{\mu_0} \left( \bar{\mathbf{B}} \otimes \bar{\mathbf{B}} - \frac{1}{2} (\bar{\mathbf{B}} \cdot \bar{\mathbf{B}}) \mathbf{I} \right). \quad (40)$$

Then, the stress components become

$$\sigma_{22}^{(r)} = \frac{G^{(r)}}{\lambda^2} + \frac{B^2}{\mu^{(r)}} - p^{(r)} = \frac{B^2}{2\mu_0}, \quad \text{and} \quad (41)$$

$$c^{(m)} \sigma_{11}^{(m)} + c^{(f)} \sigma_{11}^{(f)} = \bar{G} \lambda^2 - (c^{(m)} p^{(m)} + c^{(f)} p^{(f)}) = -\frac{B^2}{2\mu_0},$$

where  $\bar{G} = c^{(m)} G^{(m)} + c^{(f)} G^{(f)}$ . By eliminating the Lagrange multipliers  $p^{(m)}$  and  $p^{(f)}$  from Eq. (41), the relation between the applied magnetic field and induced stretch is obtained as

$$\lambda^2 - \lambda^{-2} = \frac{B^2}{\bar{G} \mu_0} \left( \tilde{\mu}_r^{-1} - 1 \right), \quad (42)$$

where  $\tilde{\mu}_r$  is the weighted harmonic mean of relative magnetic permeabilities, defined as

$$\tilde{\mu}_r = \left( \frac{c^{(m)}}{\mu_r^{(m)}} + \frac{c^{(f)}}{\mu_r^{(f)}} \right)^{-1}. \quad (43)$$

Here,  $\mu_r^{(r)} = \mu^{(r)} / \mu_0$  is the relative magnetic permeability of phase  $(r)$ . In the case of the linear magnetic layer,  $\mu_r^{(r)}$  is a constant. However, for the ferromagnetic layer,  $\mu_r^{(r)}$  can be expressed as a function of  $B$ , in terms of layer's magnetic saturation value  $m_s^{(r)}$  and the initial magnetic susceptibility  $\chi^{(r)}$  (see Eq. (28)). Hence, expression (42) is applicable for MAEs having layers with any type of magnetic behavior — linear or ferromagnetic. Equation (42) further simplifies to yield an explicit expression for  $\lambda$ , namely,

$$\lambda = \left[ \frac{\alpha + (\alpha^2 + 4)^{1/2}}{2} \right]^{1/2}, \quad (44)$$

where

$$\alpha = \frac{B^2 \left( \tilde{\mu}_r^{-1} - 1 \right)}{\bar{G} \mu_0}. \quad (45)$$

For magnetoactive layers ( $\tilde{\mu}_r > 1$ ), the application of magnetic field results in contraction along the layer direction,  $\lambda < 1$  (or  $\lambda_2 > 1$ ). We note that certain magneto-mechanical loading conditions can lead to the development of magnetoelastic instabilities [66,67]; the analysis of the magnetoelastic instabilities is provided in the next subsection.

### 3.2. Magnetoelastic instabilities

The onset of instabilities in MAE with bilayer microstructure is determined as follows. In each layer, we seek a solution for Eq. (22) of the form



$$\begin{aligned} v_i &= v_i(x_2)e^{ik_1x_1}, \quad \dot{p}(x_1, x_2) = q(x_2)e^{ik_1x_1}, \quad \text{and} \\ \dot{B}_i(x_1, x_2) &= \dot{B}_i(x_2)e^{ik_1x_1} \end{aligned} \quad (46)$$

where  $k_1$  is the wavenumber along the  $\mathbf{e}_1$ -direction. The incompressibility constraint implies

$$ik_1v_1 + v_2' = 0, \quad (47)$$

where  $(\bullet)' = (\bullet)_{,2}$ . Substitution of Eq. (46)<sub>3</sub> into the Eq. (19)<sub>2</sub> results in

$$ik_1\dot{B}_1 + \dot{B}_2' = 0. \quad (48)$$

In terms of the non-zero components of magnetoelastic tensors, the incremental governing Eq. (22) can now be written as

$$\begin{aligned} -ik_1q - k_1^2\mathcal{A}_{1111}v_1 + \mathcal{A}_{1212}v_1' + \mathcal{M}_{121}\dot{B}_1' &= 0, \\ iq' + ik_1^2\mathcal{A}_{2121}v_2 - k_1\mathcal{A}_{2222}v_1' + k_1(\mathcal{M}_{121} - \mathcal{M}_{222})\dot{B}_1 &= 0, \\ \mathcal{M}_{121}v_1' + k_1^2(\mathcal{M}_{121} - \mathcal{M}_{222})v_1 + \mathcal{H}_{11}\dot{B}_1' - ik_1\mathcal{H}_{22}\dot{B}_2' &= 0. \end{aligned} \quad (49)$$

Eqs. (47), (48), and (49) provide a set of six linear homogeneous first-order differential equations that depend on the vector of six unknown quantities  $\tilde{\mathbf{u}} = (v_1, v_1', v_2, \dot{B}_1, \dot{B}_2, q)$ . The equations can be written together as

$$\mathbf{R}\tilde{\mathbf{u}} = \tilde{\mathbf{u}}', \quad (50)$$

where the non-zero components of the matrix  $\mathbf{R}$  are given in Appendix B. The solution to Eq. (50) can be determined in the form

$$\tilde{\mathbf{u}} = \mathbf{W}\mathbf{Z}(x_2)\mathbf{u}_0, \quad (51)$$

where  $\mathbf{W}$  is the eigenvector matrix of  $\mathbf{R}$ ,  $\mathbf{Z}(x_2) = \text{diag}[\exp(\mathbf{z}x_2)]$  is a diagonal matrix. Here,  $\mathbf{z}$  is the eigenvalue vector of matrix  $\mathbf{R}$ ;  $\mathbf{u}_0$  is an arbitrary constant vector which will be determined using the continuity and quasi-periodicity conditions of the unit cell.

For the periodic unit cell of the layered composite (as shown in Fig. 2), the quasi-periodic boundary conditions are

$$\tilde{\mathbf{u}}(x_2 + L) = \tilde{\mathbf{u}}(x_2)\exp(ik_2L), \quad (52)$$

where  $k_2 \in [0, 2\pi/L]$  is the Floquet parameter. In the domain  $0 < x_2 < L + L^{(m)}$ , solution (51) takes the form

$$\begin{aligned} \tilde{\mathbf{u}}(x_2) &= \mathbf{W}\mathbf{Z}(x_2)\mathbf{u}_0^-, \quad 0 < x_2 < L^{(m)}, \\ \tilde{\mathbf{u}}(x_2) &= \mathbf{W}\mathbf{Z}(x_2)\mathbf{u}_0^f, \quad L^{(m)} < x_2 < L, \quad \text{and} \\ \tilde{\mathbf{u}}(x_2) &= \mathbf{W}\mathbf{Z}(x_2)\mathbf{u}_0^+, \quad L < x_2 < L + L^{(m)}. \end{aligned} \quad (53)$$

On substituting Eq. (53) into (52), we obtain

$$\mathbf{u}_0^+ = \exp(ik_2L)\left(\mathbf{Z}(L)\right)^{-1}\mathbf{u}_0^-. \quad (54)$$

The set of interface jump conditions for the incremental fields are

$$[[v_i]] = 0, \quad [[\dot{\sigma}]]\mathbf{L} = \mathbf{0}, \quad [[\dot{\mathbf{B}}]]\mathbf{L} = \mathbf{0}, \quad \text{and} \quad [[\dot{\mathbf{H}}]] \times \mathbf{L} = \mathbf{0}. \quad (55)$$

Using Eqs. (46), (47), and (48), the jump conditions (55) can be rewritten in terms of the components of  $\tilde{\mathbf{u}}$  as

$$\begin{aligned} [[v_1]] &= 0, \quad [[v_2]] = 0, \quad [[\dot{B}_2]] = 0, \\ [[\mathcal{M}_{121}\dot{B}_1 + ik_1pv_2 + \mathcal{A}_{1212}v_1']] &= 0, \\ [[\mathcal{M}_{222}\dot{B}_2 - ik_1(\mathcal{A}_{2222} + p)v_1 - q]] &= 0, \\ [[\mathcal{H}_{11}\dot{B}_1 + \mathcal{M}_{121}v_1' + i\mathcal{M}_{121}k_1v_2]] &= 0. \end{aligned} \quad (56)$$

Eq. (56) can be written in the form  $[[\mathbf{Q}\tilde{\mathbf{u}}]] = \mathbf{0}$ . The non-zero components of the matrix  $\mathbf{Q}$  are

$$\begin{aligned} Q_{11} &= Q_{23} = Q_{55} = -Q_{46} = 1, \quad Q_{32} = \mathcal{A}_{1212}, \quad Q_{33} = ik_1p, \\ Q_{34} &= \mathcal{M}_{121}, \quad Q_{41} = -ik_1(\mathcal{A}_{2222} + p), \quad Q_{45} = \mathcal{M}_{222}, \\ Q_{62} &= \mathcal{M}_{121}, \quad Q_{63} = ik_1\mathcal{M}_{121}, \quad Q_{64} = \mathcal{H}_{11}. \end{aligned} \quad (57)$$

Finally, by using Eq. (53) we obtain

$$\mathbf{Q}\mathbf{W}\mathbf{Z}(L^{(m)})\mathbf{u}_0^- = \mathbf{Q}\mathbf{W}\mathbf{Z}(L^{(m)})\mathbf{u}_0^f \quad \text{and} \quad \mathbf{Q}\mathbf{W}\mathbf{Z}(L)\mathbf{u}_0^+ = \mathbf{Q}\mathbf{W}\mathbf{Z}(L)\mathbf{u}_0^f. \quad (58)$$

Combining Eqs. (54) and (58) results in the following condition for the existence of a non-trivial solution

$$\det[\mathbf{K} - \exp(ik_2L)\mathbf{I}] = 0, \quad (59)$$

where

$$\mathbf{K} = \left(\mathbf{Q}\mathbf{W}\right)^{-1} \mathbf{Q}\mathbf{W}\mathbf{Z}(L^{(f)}) \left(\mathbf{Q}\mathbf{W}\right)^{-1} \mathbf{Q}\mathbf{W}\mathbf{Z}(L^{(m)}). \quad (60)$$

Thus, if the condition (59) is satisfied for a combination of mechanical and magnetic loads, a solution of the form (46) exists. The solution  $\tilde{\mathbf{u}}$  lies in the real space, and from Eq. (52),  $\exp(ik_2L)$  is also real-valued; hence, non-trivial solutions are  $\exp(ik_2L) = \pm 1$ . The instability criterion (59) is evaluated with scanning over the values of  $k_1$  at different deformation levels for a given magnetic field until the eigenvalue with  $|\exp(ik_2L)| = 1$  is obtained. Once the condition is satisfied, the corresponding stretch along the direction of layers ( $\mathbf{e}_1$ ) that separates the unstable and stable domain (illustratively shown in Fig. 6a) is termed as the critical stretch  $\lambda_{cr}$  and the corresponding wavenumber is the critical wavenumber  $k_{1cr}$ .

Based on the buckling pattern wavelength, we distinguish the macroscopic (or long-wave) and microscopic instabilities. Macroscopic instability is characterized by the critical wavelength significantly larger than the characteristic microstructure ( $k_{1cr} \rightarrow 0$ ), whereas microscopic instability may lead to the formation of a new periodicity of the order of the initial microstructure (see [48] for the purely mechanical case). Furthermore, depending on the two possible values of eigenvalue:  $\exp(ik_2L) = 1$  and  $-1$ , the buckling modes can be classified as symmetric for  $k_2L = 2n\pi$  and antisymmetric for  $k_2L = (2n-1)\pi$  (with  $n$  being an integer). For illustrating these instability modes in the plots, hereafter, we use  $k_2L = 2\pi$  and  $k_2L = \pi$  (with  $n = 1$ ) to represent the symmetric and antisymmetric modes, respectively. These buckling modes are schematically shown in Fig. 3.

#### 4. Examples

In this section, we illustrate the analysis through the examples for the laminate MAEs with magnetically inactive matrix (i.e.,  $\chi^{(m)} = 0$ ), and different magnetic behaviors of the stiffer active layer. In the discussion hereafter, we denote the magnetic parameters corresponding to the stiffer active layer without the superscript  $(f)$ .

##### 4.1. Magnetostriction in layered MAEs

In this subsection, we analyze the magnetic field induced deformation in the layered MAEs. In Fig. 4, we plot the field-induced stretch as the function of normalized magnetic induction  $B_m = B/\sqrt{G^{(m)}\mu_0}$ . Here,  $\lambda_{mag}$  is the stretch induced along the direction of applied magnetic field ( $\mathbf{e}_2$ ), which is determined using Eq. (44) as  $\lambda_{mag} = \lambda_2 = \lambda^{-1}$ . The results are shown for MAEs with stiff layer volume fraction  $c^{(f)} = 0.4$ , initial magnetic susceptibility  $\chi = 0.9$ , and initial shear modulus contrast  $G^{(f)}/G^{(m)} = 10$ . The black solid curve denotes the response of the MAE with the stiff layer characterized by the linear magnetic behavior. For the stiff layer with ferromagnetic behavior, we consider three magnetic saturation values:  $m_s\mu_0 = 10$  T (green dashed curve),  $m_s\mu_0 = 5$  T (blue dotted curve), and  $m_s\mu_0 = 2$  T (red dash-dotted curve).

Clearly, the magnetic field induced stretch  $\lambda_{mag}$  increases with an

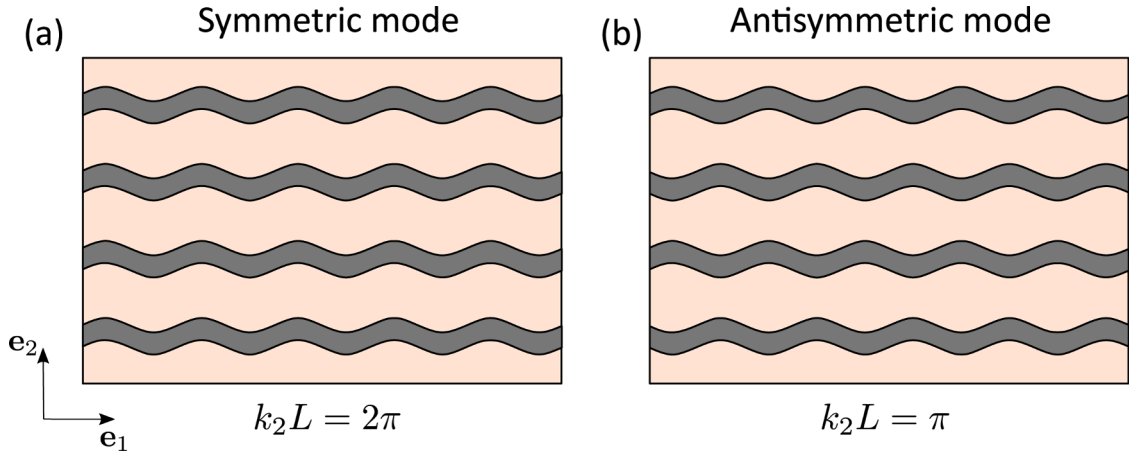


Fig. 3. Schematic representation of the symmetric (a) and antisymmetric (b) microscopic instability modes.

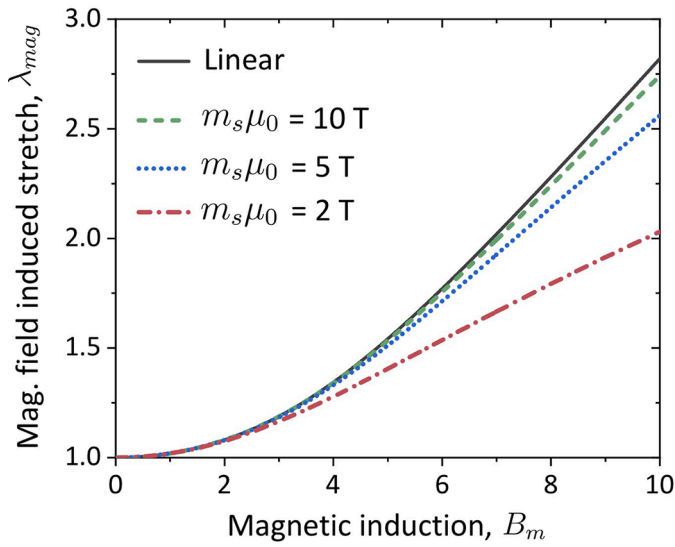


Fig. 4. Magnetic field-induced stretch  $\lambda_{mag} = \lambda_2$  as the function of normalized magnetic induction  $B_m = B/\sqrt{G^{(m)}}/\mu_0$ . MAE with stiff layer's volume fraction  $c^{(f)} = 0.4$ , initial magnetic susceptibility  $\chi = 0.9$ , and initial shear modulus contrast  $G^{(f)}/G^{(m)} = 10$  are considered.

increase in the applied magnetic field for both the MAEs with linear magnetic and ferromagnetic behaviors. We observe that MAE with the linear magnetic behavior undergoes larger deformations as compared to those with the ferromagnetic behavior. For instance, at  $B_m = 7$ , the induced stretch corresponding to linear magnetic MAE is  $\lambda_{mag} = 2.01$ , whereas in MAE with  $m_s\mu_0 = 2$  T it is  $\lambda_{mag} = 1.66$ . Moreover, among the MAEs with ferromagnetic behavior, the stretch  $\lambda_{mag}$  decreases with a decrease in magnetic saturation value. For example, at  $B_m = 10$ , the magnetic field-induced stretch decreases from  $\lambda_{mag} = 2.74$  to  $\lambda_{mag} = 2.03$  as magnetic saturation decreases from  $m_s\mu_0 = 10$  T to  $m_s\mu_0 = 2$  T (see green and red curves).

The observed dependence of magneto-deformation on  $m_s\mu_0$  values is due to the variation in MAE's effective magnetic permeability. In particular, with the decrease in the magnetic saturation values, the effective magnetic permeability also decreases (28), leading to an increase in the contribution of magnetic stress into the total stress, Eq. (38). However, Maxwell's stress  $\sigma_m^*$  does not change with MAE's magnetic properties, and to satisfy the mechanical traction-free boundary conditions, the total stress inside the MAE also remains constant, Eq. (39). Therefore, an increase in magnetic stress is compensated by a

decrease in mechanical stress. Thus, the MAE undergoes comparatively smaller deformations as the active layer's magnetic saturation value decreases.

Next, in Fig. 5, we plot the magnetic field induced stretch as the function of stiff active layer volume fraction  $c^{(f)}$ . The MAEs with  $\chi = 0.9$  are subjected to the magnetic field of magnitude  $B_m = 10$ . Similar to Fig. 4, in Fig. 5a, we consider the ferromagnetic MAEs with  $G^{(f)}/G^{(m)} = 10$  having different magnetic saturation values. For completeness, we show the results for linear magnetic MAEs with different shear modulus contrasts in Fig. 5b.

We observe that the field-induced stretch monotonically increases with an increase in  $c^{(f)}$ , regardless of MAE's magnetic behavior (see Fig. 5a) and shear modulus contrast (see Fig. 5b). This is because, only the stiff layer contributes to the response of MAEs under the applied magnetic field. Similar to the observations in Fig. 4, the induced stretch is higher for linear magnetic behavior, and  $\lambda_{mag}$  decreases with a decrease in  $m_s\mu_0$ . As expected, the magnetic field induced deformation decreases with an increase in shear modulus contrast (see Fig. 5b).

#### 4.2. Magnetoelastic instabilities in layered MAEs

In this subsection, we analyze the magnetoelastic instabilities in MAEs with bilayered microstructure. First, we investigate the effect of the applied magnetic field  $B_m$  on the critical stretch  $\lambda_{cr}$  and wavenumber  $k_{cr}$ , and related instability modes. Here,  $\lambda_{cr}$  denotes the critical stretch value ( $\lambda_1$  along the direction of layers  $e_1$ ) corresponding to the onset of instability. In the second part of this subsection, we examine the role of phase volume fraction in the development of instabilities in MAEs with different magnetic behaviors. In the following examples, we consider the MAEs with initial shear modulus contrast  $G^{(f)}/G^{(m)} = 10$ .

##### 4.2.1. Effect of magnetic field on magnetoelastic instabilities

We start by illustrating the influence of the applied magnetic field on the stability of MAEs with linear magnetic behavior. Fig. 6 shows the critical stretch (a) and normalized critical wavenumbers:  $k_1^*$  and  $k_2^*$  (b) as the functions of normalized magnetic induction  $B_m$ . The wavenumbers are normalized with respect to the period length  $L$  in the current configuration (see Fig. 2) as  $k_1^* = k_1L$  and  $k_2^* = k_2L$ . We consider the MAEs with stiff layer volume fraction  $c^{(f)} = 0.6$  and initial magnetic susceptibility  $\chi = 0.95$ . Here and thereafter, we use solid and dotted curves for macroscopic and microscopic instabilities, respectively (see Fig. 6a). Furthermore, solid and dash-dotted curves denote the critical wavenumbers  $k_1^*$  and  $k_2^*$ , respectively (see Fig. 6b).

We find that the critical stretch increases with an increase in the applied magnetic field. Furthermore, we observe that when the MAE is subjected to a smaller magnetic field ( $B_m \leq 2.5$ ), it develops instabilities

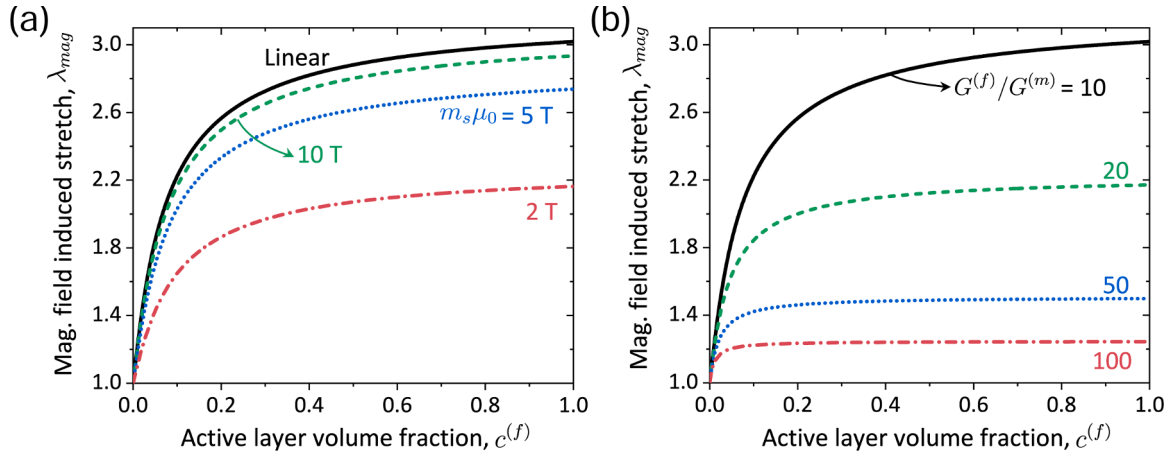


**Fig. 5.** Magnetic field induced stretch  $\lambda_{mag} = \lambda_2$  as the function of active layer volume fraction  $c^{(f)}$ . The results are shown for (a) ferromagnetic MAEs with  $G^{(f)}/G^{(m)} = 10$  and (b) linear magnetic MAEs with different shear modulus contrast values. MAEs with initial magnetic susceptibility  $\chi = 0.9$  are subjected to magnetic field  $B_m = 10$ .

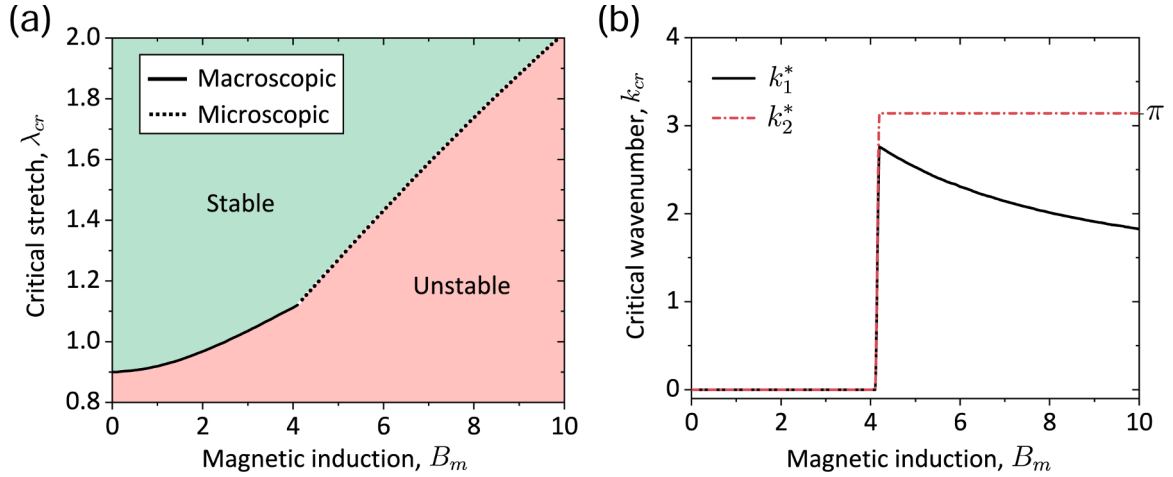


**Fig. 6.** Critical stretch  $\lambda_{cr}$  (a) and normalized critical wavenumbers (b) vs. the normalized magnetic field  $B_m$ . MAEs with stiff layer's volume fraction  $c^{(f)} = 0.6$  and initial magnetic susceptibility  $\chi = 0.95$ .

under compressive strains ( $\lambda_{cr} < 1$ ). Interestingly, at higher magnetic fields, MAE is unstable even under tensile strains. For example, the MAE is unstable for  $\lambda < 1.59$ , when subjected to  $B_m = 7$ . Moreover, we find that the instability mode switches at a certain threshold magnitude of magnetic induction  $B_m^{th}$ . In particular, macroscopic instability appears for  $B_m < B_m^{th}$ , whereas microscopic instability emerges for  $B_m > B_m^{th}$ . For the considered MAE, the threshold value is  $B_m^{th} = 4.1$ .

The transition in the instability mode is also evident from the evolution of the critical wavenumbers ( $k_1^*$  and  $k_2^*$ ) with the magnetic field (see Fig. 6b). For  $B_m > B_m^{th}$ , the wavenumbers have finite non-zero values, hence, representing the microscopic instability. In particular, the MAEs develop an antisymmetric mode of microscopic instability, as the critical wavenumber  $k_2^* = \pi$ , when subjected to this range of magnetic field values (see Fig. 6b). Moreover, we find that the wavenumber  $k_1^*$  monotonically decreases with an increase in  $B_m$ , hence, showing the tunability of buckling patterns with an applied magnetic field. For magnetic induction magnitudes smaller than  $B_m^{th}$ , both the critical wavenumbers ( $k_1^*$  and  $k_2^*$ ) approach zero,  $k_{cr} \rightarrow 0$ , showing the long-wave or macroscopic loss of stability.

Next, we investigate the development of magnetoelastic instabilities in MAEs with ferromagnetic behavior. Fig. 7 shows the critical stretch (a),(c), and critical wavenumbers (b),(d) as functions of  $B_m$  for MAEs

with  $\chi = 0.95$ . The results are shown for MAEs with stiff layer volume fractions:  $c^{(f)} = 0.4$  (Fig. 7a and b) and (Fig. 7c and d). We consider the MAEs with magnetic saturation values:  $m_s\mu_0 = 10$  T (blue curves),  $m_s\mu_0 = 5$  T (red curves), and  $m_s\mu_0 = 2$  T (green curves). The results for MAEs with the linear magnetic behavior are included for comparison (black curves).

Similar to MAEs with linear magnetic behavior, the MAEs with ferromagnetic behavior also develop instabilities at higher stretches when subjected to higher magnetic fields. However, we observe that the critical stretch, at a particular magnetic induction magnitude, decreases with a decrease in the MAE magnetic saturation value. For example, in MAEs with  $c^{(f)} = 0.4$  at  $B_m = 8$ , the critical stretches (with corresponding magnetic saturation values) are  $\lambda_{cr} = 1.55$  ( $m_s\mu_0 = 10$  T),  $\lambda_{cr} = 1.22$  ( $m_s\mu_0 = 5$  T), and  $\lambda_{cr} = 0.96$  ( $m_s\mu_0 = 2$  T); for linear magnetic behavior,  $\lambda_{cr} = 1.88$ . Moreover, the critical stretches of MAEs with smaller magnetic saturation values, for example,  $m_s\mu_0 = 5$  T and  $m_s\mu_0 = 2$  T, approach a saturation value at higher values of  $B_m$  (see the red and green curves in Fig. 7a and c). These observations hold regardless of the volume fraction of phases.

The effect of the applied magnetic field on the buckling patterns and instability modes strongly depends on the stiff layer volume fraction and its magnetic behavior. First, consider the MAEs with a high stiff layer volume fraction,  $c^{(f)} = 0.4$ . We observe that in these MAEs, the



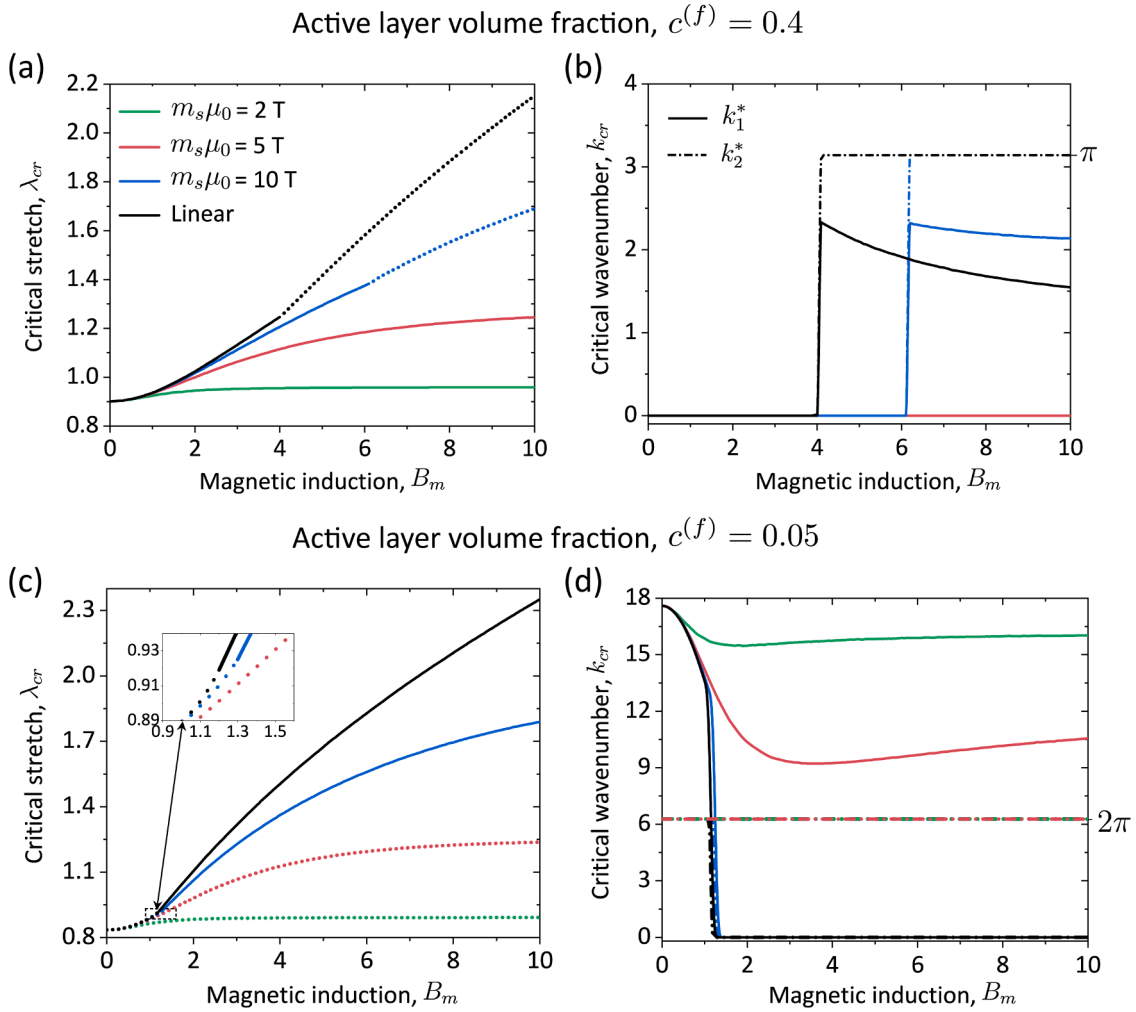


**Fig. 7.** Critical stretch  $\lambda_{cr}$  (a),(c), and normalized critical wavenumbers (b),(d) vs. the normalized magnetic field  $B_m$ . MAEs with stiff layer's initial magnetic susceptibility  $\chi = 0.95$  and volume fractions:  $c^{(f)} = 0.4$  (a),(b) and  $c^{(f)} = 0.05$  (c),(d) are considered.

threshold magnetic induction  $B_m^{th}$ , at which the instability mode switches, increases with a decrease in  $m_s\mu_0$ . Thus, the MAEs composites with lower magnetic saturations favor the long instability over the microscopic one. For the considered MAEs, the transition occurs at  $B_m^{th} = 4$  (linear) and  $B_m^{th} = 6.1$  ( $m_s\mu_0 = 10$  T). Interestingly, the MAEs with magnetic saturation values  $m_s\mu_0 = 5$  T and  $m_s\mu_0 = 2$  T do not show any transition in the considered range of  $B_m$ , and develop macroscopic instabilities. We find that the MAEs with  $c^{(f)} = 0.4$  develop the antisymmetric mode of microscopic instabilities ( $k_2^* = \pi$ ), for both magnetic behaviors. However, the wavelength of the buckling pattern is smaller (higher  $k_1^*$ ) in MAEs with the ferromagnetic behavior as compared to linear ones, when they are to develop microscopic instabilities (see the black and blue curves in Fig. 7b).

The MAEs with smaller volume fraction,  $c^{(f)} = 0.05$ , develop microscopic instabilities when subjected to smaller magnitudes of the magnetic field. The instability mode switches to macroscopic at magnitudes  $B_m > B_m^{th}$  (see Fig. 7c and d). Moreover, the threshold magnitude  $B_m^{th}$  increases with a decrease in  $m_s\mu_0$  (see inset in Fig. 7c). However, for smaller magnetic saturation values,  $m_s\mu_0 = 5$  T and  $m_s\mu_0 = 2$  T, the transition in the instability mode does not occur in the considered range of the applied magnetic field. Hence, as opposed to MAEs with high volume fractions ( $c^{(f)} = 0.4$ ), in MAEs with  $c^{(f)} = 0.05$ , a decrease in magnetic saturation values promotes microscopic (or finite-wavelength) instabilities. Moreover, these MAEs develop the symmetric mode of

microscopic instability, with the critical wavenumber  $k_2^* = 2\pi$  (see the dash-dotted curves in Fig. 7d).

The results indicate that in addition to the influence of the applied magnetic field and phase magnetic behavior, the instability development and associated buckling patterns significantly depend on the volume fraction of layers. A detailed analysis of the effect of phase volume fractions is provided in Section 4.2.2.

Next, we study the influence of initial magnetic susceptibility on the magnetoelastic instabilities in the ferromagnetic layered MAEs. To this end, in Fig. 8, we show the critical parameters corresponding to MAEs with initial magnetic susceptibilities:  $\chi = 0.95$  (a), (b);  $\chi = 0.80$  (c), (d); and  $\chi = 0.375$  (e). The results are shown for MAEs with stiff layer volume fraction  $c^{(f)} = 0.4$ .

The critical stretch decreases with a decrease in the initial magnetic susceptibility; this is observed for all magnetic saturation values. For instance, the critical stretch at  $B_m = 10$  corresponding to MAEs with  $m_s\mu_0 = 10$  T decreases from  $\lambda_{cr} = 1.69$  to  $\lambda_{cr} = 1.10$  as susceptibility varies from  $\chi = 0.95$  to  $\chi = 0.375$  (compare the blue curves in Fig. 8a and e). Moreover, the critical wavenumber  $k_1^*$  increases with a decrease in  $\chi$ , in the MAEs that develop microscopic instabilities. We note that the effect of initial magnetic susceptibility on the critical parameters,  $\lambda_{cr}$  and  $k_{cr}$ , is similar to that observed in the case of magnetic saturation values (see Fig. 7a and b). This is because a decrease in magnetic saturation and/or initial magnetic susceptibility values leads to a decrease in MAE's magnetization and vice-versa, at a given magnetic field

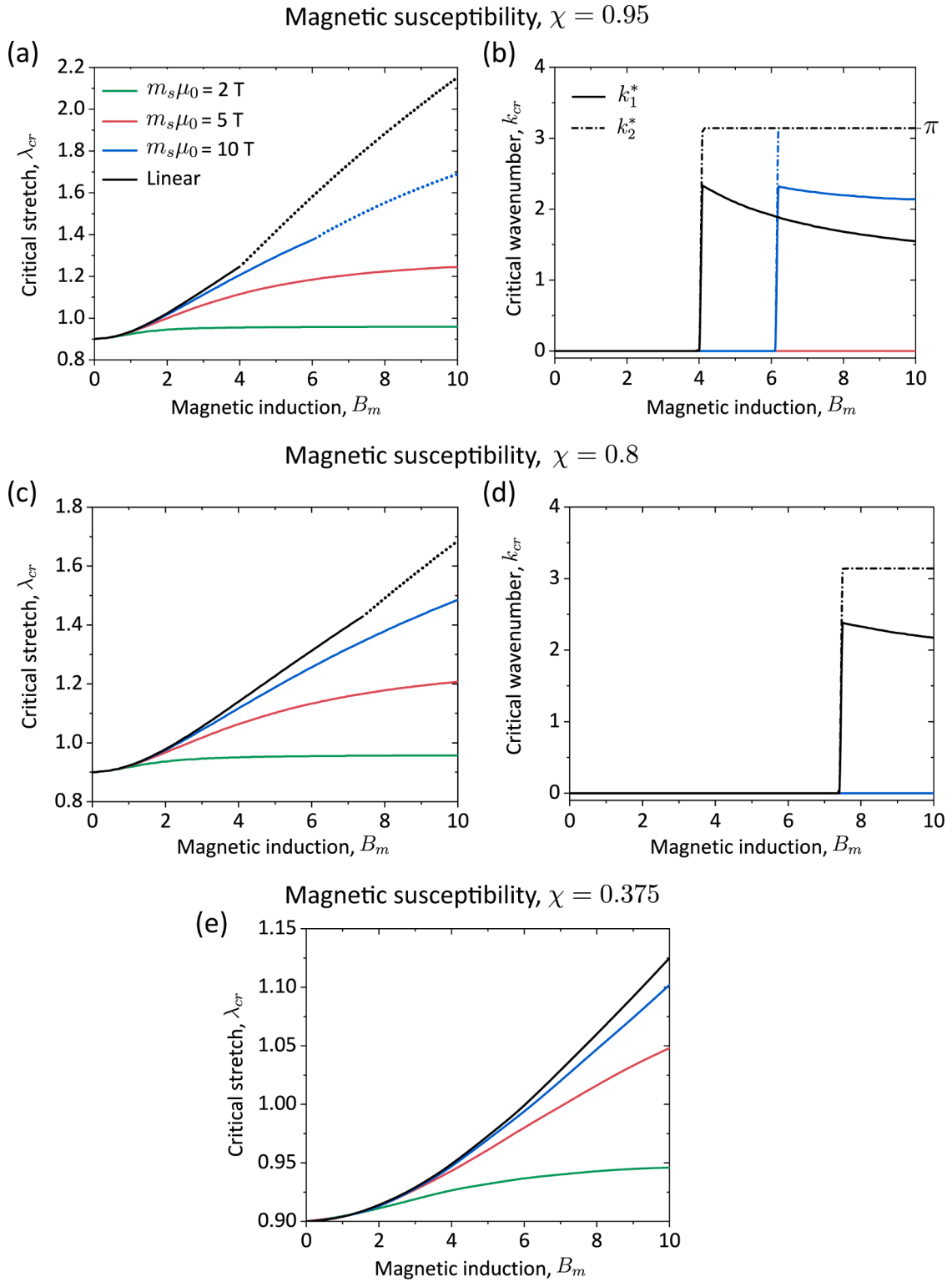


**Fig. 8.** Critical stretch  $\lambda_{cr}$  (a),(c),(e) and normalized critical wavenumbers (b),(d) vs. the normalized magnetic field  $B_m$ . MAEs with stiff layer's volume fraction  $c^{(f)} = 0.4$  and initial magnetic susceptibilities:  $\chi = 0.95$  (a), (b);  $\chi = 0.80$  (c), (d); and  $\chi = 0.375$  (e) are considered.

magnitude.

The initial magnetic susceptibility also significantly influences the instability mode in the MAEs. In particular, lower values of  $\chi$  favor the occurrence of macroscopic instabilities in MAEs. For instance, in the linear magnetic MAEs the threshold magnetic induction, at which the instability mode switches, increases from  $B_m^{th} = 4$  to  $B_m^{th} = 7.4$  as susceptibility changes from  $\chi = 0.95$  to  $\chi = 0.80$ . For further smaller

magnetic susceptibilities, for example,  $\chi = 0.375$ , no transition in the instability mode is observed, and the MAEs develop macroscopic instabilities, regardless of their magnetic behavior (see Fig. 8e).

#### 4.2.2. Effect of volume fraction of phases on magnetoelastic instabilities

Here, we study the effect of the phase volume fraction on the magnetoelastic instabilities. First, we examine the linear magnetic MAEs

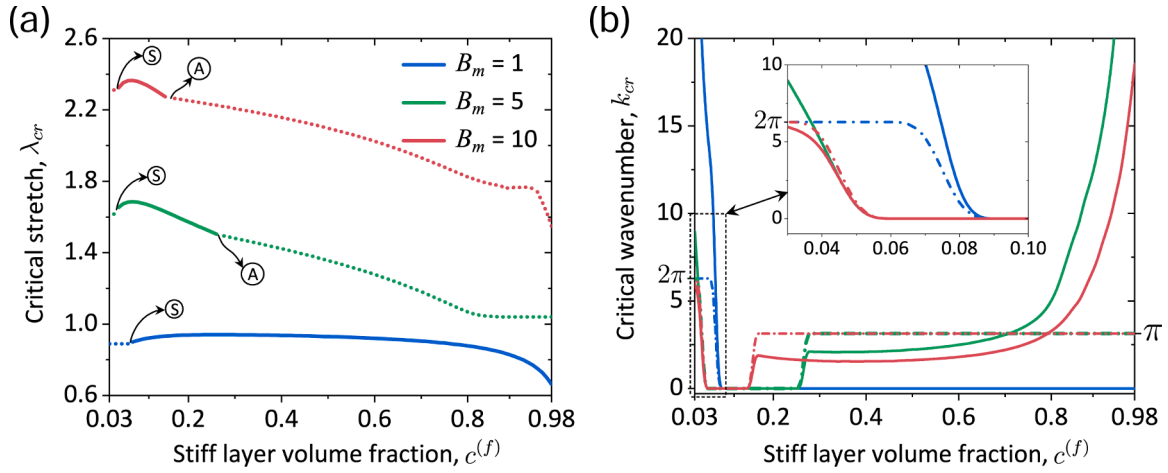


**Fig. 9.** Critical stretch  $\lambda_{cr}$  (a) and normalized critical wavenumbers (b) vs. the stiff layer volume fraction  $c^{(f)}$ . Linear magnetic MAEs with  $\chi = 0.95$  are subjected to  $B_m = 1$ ,  $B_m = 5$ , and  $B_m = 10$ .

with  $\chi = 0.95$ . In Fig. 9, we plot the critical stretch (a) and wavenumber (b) as the functions of stiff layer volume fraction  $c^{(f)}$ . We consider the MAEs subjected to  $B_m = 1$  (blue curves),  $B_m = 5$  (green curves), and  $B_m = 10$  (red curves). For the sake of convenient discussion, in Fig. 9a, we have marked the first and second instability mode transition points as ‘S’ and ‘A’, respectively. In particular, ‘S’ represents the switch from *symmetric* microscopic instability mode to macroscopic, whereas ‘A’ denotes the transition from macroscopic to *antisymmetric* microscopic instability, with an increase in  $c^{(f)}$ .

For the MAEs subjected to smaller magnetic field levels, for example,  $B_m = 1$ , the critical stretch increases with an increase in  $c^{(f)}$  up to a certain value; beyond that volume fraction value, the critical stretch decreases with a further increase in the volume fraction. Moreover, when the stiff layer volume fraction is smaller than a particular threshold value,  $c_{th}^{(f)}$ , the MAEs develop symmetric microscopic buckling modes ( $k_2^* = 2\pi$ ). However, at higher values of  $c^{(f)}$ , a macroscopic loss of stability occurs. We also observe that the wavelength of the buckling pattern increases ( $k_1^*$  decreases) with an increase in  $c^{(f)}$ , and it approaches the long-wave limit ( $k_1^* \rightarrow 0$ ) for  $c^{(f)} \geq c_{th}^{(f)}$ . The corresponding threshold value is  $c_{th}^{(f)} = 0.07$ , which is marked as ‘S’ on the blue curve (see Fig. 9a). We note that similar variation of critical parameters with stiff layer volume fraction has also been reported for layered composites subjected to purely mechanical loadings [55].

However, MAEs subjected to higher magnetic induction values show contrastingly different instability mode transitions and highly non-monotonous variation of critical parameters. For example, consider the MAEs under  $B_m = 5$ ; these MAEs, similar to MAE under  $B_m = 1$ , also show the first transition ‘S’ in the instability mode. Interestingly, these MAEs undergo an additional transition, back to microscopic instability, at higher values of  $c^{(f)}$ ; this shift in the instability mode is marked as ‘A’ on the green curve in Fig. 9a. Both transitions are also evident from the evolution of critical wavenumbers with stiff layer volume fraction (see the green curves in Fig. 9b). Furthermore, we observe that in the MAEs developing microscopic instabilities, the critical wavelength significantly varies with the volume fraction. This high tunability of wavelength (or  $k_1^*$ ) is very pronounced in the vicinity of the extreme volume fraction values, i.e.,  $c^{(f)} \rightarrow 0$  and  $c^{(f)} \rightarrow 1$  (see Fig. 9b).

Remarkably, the morphologies of MAEs that are to develop micro-

scopic instabilities, can exhibit antisymmetric and symmetric instability modes with distinct values for critical wavenumber  $k_2^*$ , dictated by the stiff layer volume fraction. In particular, MAEs with  $c^{(f)}$  smaller than that corresponding to first transition point ‘S’, i.e.,  $c^{(f)} < c_{th}^{(f)}$ , has  $k_2^* = 2\pi$ . However, for stiff layer volume fraction higher than that of,  $c^{(f)} > c_{th}^{(f)}$ , has  $k_2^* = \pi$  (see green dash-dotted curve). Similar behavior is observed for MAEs subjected to  $B_m = 10$  (see the red curves). Thus, at high magnetic field magnitudes, MAEs with smaller  $c^{(f)}$  develop *symmetric* mode of microscopic instability, long-wave instability emerges at moderate values of  $c^{(f)}$ , and microscopic instability with *antisymmetric* buckling pattern arises at higher stiff layer volume fractions.

The threshold stiff layer volume fractions for both transition points decrease with an increase in the magnitude of the applied magnetic field. For example, the threshold  $c_{th}^{(f)}$  corresponding to the ‘S’ transition point decreases from  $c_{th}^{(f)} = 0.07$  to  $c_{th}^{(f)} = 0.04$  as the applied magnetic field changes from  $B_m = 1$  to  $B_m = 5$ . Moreover, the threshold values for ‘A’ decreases from  $c_{th}^{(f)} = 0.25$  (at  $B_m = 5$ ) to  $c_{th}^{(f)} = 0.14$  (at  $B_m = 10$ ). Hence, the application of a strong magnetic field favors the occurrence of the antisymmetric mode of microscopic instability.

Next, we study the effect of volume fraction in MAEs with ferromagnetic behavior. Fig. 10 shows the critical stretch (a) and critical wavenumbers (b) versus stiff layer volume fraction for the MAEs with magnetic saturation values  $m_s\mu_0 = 10$  T (blue curves) and  $m_s\mu_0 = 5$  T (red curves). We consider the MAEs with  $\chi = 0.95$  subjected to magnetic induction  $B_m = 10$ . The results for the linear magnetic MAEs are denoted by the black curves and are added for comparison.

We observe that the instability in ferromagnetic MAEs develops at smaller stretches than in their linear magnetic counterparts. Among the ferromagnetic MAEs, the lesser the magnetic saturation value, the smaller is the critical stretch. Moreover, the critical wavelength (wavenumber) decreases (increases) with a decrease in  $m_s\mu_0$ . These findings are consistent with the previous observations in Fig. 7. Similar to the linear magnetic MAEs, ferromagnetic MAEs also offer a high tunability of the critical wavenumber  $k_1^*$ , especially in the vicinity of the extreme volume fraction values (see Fig. 10b).

Comparing the critical parameters of ferromagnetic MAEs (Fig. 10) with those of linear magnetic MAEs (in Fig. 9), we find that a decrease in

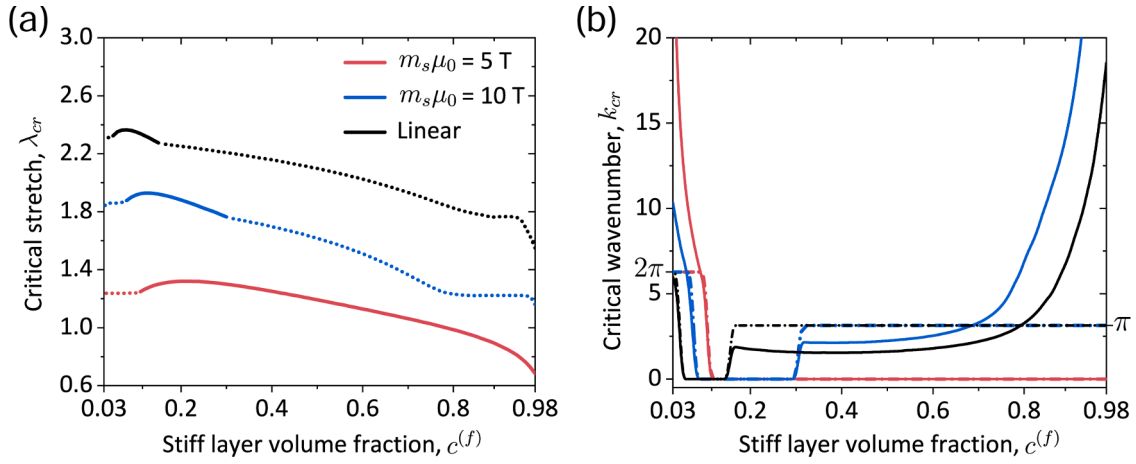


**Fig. 10.** Critical stretch  $\lambda_{cr}$  (a) and normalized critical wavenumbers (b) vs. the stiff layer volume fraction  $c^{(f)}$ . Linear magnetic MAEs with  $\chi = 0.95$  are subjected to  $B_m = 10$ . The results are shown for ferromagnetic MAEs with  $m_s\mu_0 = 5$  T and  $m_s\mu_0 = 10$  T, together with linear magnetic MAEs.

the magnetic field magnitude (in linear MAEs) has a similar influence as decreasing the magnetic saturation value (in ferromagnetic MAEs under a constant magnetic field). This occurs because of the magnetic saturation effect present in the ferromagnetic MAEs. In particular, the saturation effect takes place at smaller magnetic fields in MAEs with small saturation values. Therefore, when subjected to higher values of  $B_m$ , the influence of the applied magnetic field on the magnetoelastic tensors of ferromagnetic MAEs is significantly weaker than that in their magnetically linear counterparts.

The transition of instability modes also demonstrates the behavior resembling that in Fig. 9. For instance, MAEs with smaller saturation values ( $m_s\mu_0 = 5$  T) have only the first transition point ‘S’, whereas MAEs with higher saturation value ( $m_s\mu_0 = 10$  T) show two transitions. Moreover, the threshold values corresponding to the transitions decrease with an increase in  $m_s\mu_0$ . For example, the ‘A transition occurs at  $c^{(f)} = 0.3$  (for  $m_s\mu_0 = 10$  T) and  $c^{(f)} = 0.15$  (for linear magnetic). The ‘S transition in MAEs with  $m_s\mu_0 = 5$  T and  $m_s\mu_0 = 10$  T occurs at  $c^{(f)} = 0.1$  and  $c^{(f)} = 0.07$ , respectively. Hence, the MAEs with smaller values of  $m_s\mu_0$  are less likely to develop antisymmetric microscopic instabilities.

Finally, we illustrate the influence of the initial magnetic susceptibilities on the critical parameters and instability mode transition with phase volume fraction. Fig. 11 shows the critical parameters for linear magnetic MAEs with  $\chi = 0.95$  (black curves),  $\chi = 0.80$  (blue curves), and  $\chi = 0.375$  (red curves). We consider the MAEs subjected to magnetic inductions  $B_m = 1$  (Fig. 11a and b),  $B_m = 5$  (Fig. 11c and d), and  $B_m = 10$  (Fig. 11e and f).

Consistent with the findings in Fig. 8, we observe that the MAEs with lower values of  $\chi$  develop instabilities at smaller stretch levels. Moreover, the critical wavenumber  $k_1^*$  decreases with an increase in  $\chi$ , in the MAEs that develop microscopic instabilities. This holds independent of the magnitude of magnetic induction.

The interplay between the instability modes is also dictated by the magnetic susceptibility of the MAEs. In particular, we observe that the threshold value corresponding to the transition point ‘S’ increases with a decrease in  $\chi$ , irrespective of the magnetic fields magnitude. For example, under  $B_m = 5$ , the transition ‘S’ occurs at  $c^{(f)} = 0.04$  (for  $\chi = 0.95$ ),  $c^{(f)} = 0.07$  (for  $\chi = 0.80$ ), and  $c^{(f)} = 0.13$  (for  $\chi = 0.375$ ). Moreover, we find that the occurrence of the second switch in instability mode with  $c^{(f)}$  depends on the value of  $\chi$ , together with the magnetic

field. For instance, ‘A transition point is not observed for any of the MAEs subjected to  $B_m = 1$ . Under  $B_m = 5$ , however, ‘A transition only takes place for MAEs with  $\chi = 0.95$ . For MAEs subjected to  $B_m = 10$ , the second switch in instability mode is observed for  $\chi = 0.95$  and  $\chi = 0.80$ . Similar to ‘S instability transition, for ‘A transition, the threshold volume fraction increases with a decrease in  $\chi$ . For example, the corresponding threshold values for MAEs under  $B_m = 10$  are  $c^{(f)} = 0.15$  (for  $\chi = 0.95$ ) and  $c^{(f)} = 0.32$  (for  $\chi = 0.80$ ).

## 5. Conclusion

In this paper, we investigated the behavior of MAEs with bi-phasic layered microstructure with ferromagnetic hyperelastic phases. We considered the MAE laminates subjected to a magnetic field perpendicular to the direction of layers. First, we derived an explicit expression for the field-induced stretch in response to the remotely applied magnetic field. Second, we performed the magnetoelastic instability analysis for layered MAEs, by employing the small amplitude perturbation superimposed on finite deformations in the presence of a magnetic field. While the formulation developed here is general – for any magnetic behavior of phases, the results are presented for the special class of MAEs with magnetically inactive matrix and active stiff layer phase.

We found that the layered MAEs experience tension along the direction of the magnetic field, and the induced stretch increases with an increase in the applied magnetic field. However, because of the magnetic saturation effect, the MAEs with smaller saturation values attain smaller deformation levels. We also showed that the MAEs with higher volume fractions of the active phase develop large deformations, irrespective of shear modulus contrast between the phases.

The layered MAEs, when subjected to higher magnitudes of the magnetic field, develop instabilities at higher stretches along the direction of layers (perpendicular to the magnetic field). In fact, MAEs are observed to be unstable even under tensile strains in the presence of a strong magnetic field. The magnetic saturation effect, however, results in a decrease of critical stretch levels. Moreover, the wavelength of buckling patterns is shown to be highly tunable by the applied magnetic field. The comparison of critical parameters – for MAEs with various morphologies – shows that a decrease in magnetic susceptibility and/or magnetic saturation values (at a given magnetic field magnitude) has a similar response as reducing the applied magnetic field magnitude.

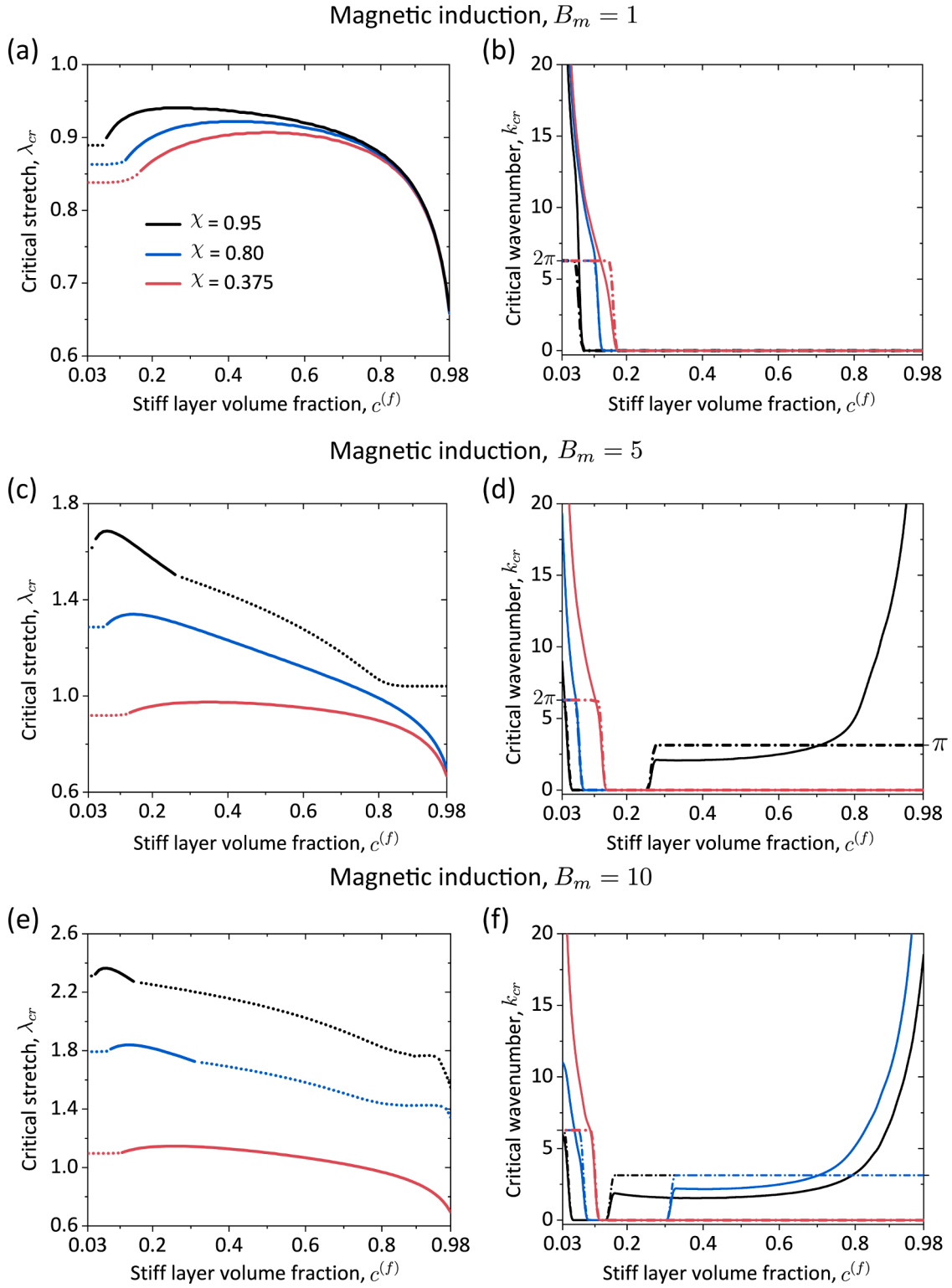


**Fig. 11.** Critical stretch  $\lambda_{cr}$  (a),(c),(e) and normalized critical wavenumbers (b), (d), (f) vs. the stiff layer volume fraction  $c^{(f)}$ . Linear magnetic MAEs with initial magnetic susceptibilities  $\chi = 0.95$ ,  $\chi = 0.80$ , and  $\chi = 0.375$  are subjected to  $B_m = 1$  (a), (b);  $B_m = 5$  (c), (d); and  $B_m = 10$  (e), (f).

The instability mode and their transitions in layered MAEs are strongly dictated by the volume fraction of phases together with the applied magnetic field. In the presence of a weak magnetic field, similar

to the purely mechanical case of layered composites, the layered MAEs also show the transition in instability modes once, with the change in volume fraction. Thus, the symmetric microscopic instability occurs at



small volume fractions of the active stiff phase, whereas macroscopic loss of stability occurs at higher volume fractions. Under higher magnetic fields, however, the MAE laminates show two transitions with three distinct instability modes at different active phase volume fractions. First, the symmetric microscopic instability is detected at smaller volume fractions. Second, at moderate volume fractions, the long-wave instability emerges. Interestingly, the MAEs with higher volume fractions develop microscopic instability with *antisymmetric* buckling patterns. We found that under stronger magnetic fields, the range of active stiff phase volume fractions, at which the antisymmetric mode is attained, further increases. Hence, the application of magnetic field promotes the development of the antisymmetric buckling patterns. It is worth noting that the antisymmetric microscopic instability mode is inadmissible in the purely mechanical setting (without a magnetic field).

The presented results can help widen the design space for novel materials with switchable functionalities with potential applications in remotely controlled soft microactuators and sensors. Moreover, the theoretically predicted antisymmetric buckling mode can motivate further experimental studies of the microstructured MAEs. In the study, we have considered the MAEs subjected to quasi-static loading; therefore, the viscous and inertial effects have not been considered. However, for the dynamic loading, these effects can influence the material

stability, as observed, for example, in the soft laminates [76]. To investigate of the influence of time-dependent magneto-mechanical loading on the instability development in MAEs, one should account for the phase rate-dependent behavior and inertia in the modeling. Additionally, the understanding of the material behavior can benefit from the implementation of multiscale modeling that could more accurately capture the global finite size effects, as well as smaller length-scale effects (such as, for example, dipole-dipole interactions).

### Declaration of Competing Interest

The authors declare that they have no known competing financial interests or personal relationships that could have appeared to influence the work reported in this paper.

### Acknowledgment

The authors acknowledge the start-up support of the University of Wisconsin-Madison. NA thank the support through LeRoy fellowship. SR is grateful for the support of European Research Council (ERC) through Grant No. 852281 - MAGIC.

## Appendix A. Magnetoelastic moduli tensors

For the layer  $(r) \in \{m, f\}$  exhibiting linear magnetic behavior, the non-zero components of magnetoelastic moduli tensors are

$$\begin{aligned} \mathcal{A}_{1111}^{(r)} &= \mathcal{A}_{2121}^{(r)} = G^{(r)} \lambda^2, \\ \mathcal{A}_{1212}^{(r)} &= \mathcal{A}_{2222}^{(r)} = G^{(r)} \lambda^{-2} + B^2 / (\mu^{(r)} \mu_0), \end{aligned} \quad (\text{A.1})$$

$$\mathcal{H}_{11}^{(r)} = \mathcal{H}_{22}^{(r)} = (\mu^{(r)} \mu_0)^{-1}, \quad (\text{A.2})$$

and

$$\begin{aligned} \mathcal{M}_{121}^{(r)} &= \mathcal{M}_{211}^{(r)} = B(\mu^{(r)} \mu_0)^{-1} \\ \mathcal{M}_{222}^{(r)} &= 2B(\mu^{(r)} \mu_0)^{-1}. \end{aligned} \quad (\text{A.3})$$

For ferromagnetic behavior, the components of tensors are

$$\begin{aligned} \mathcal{A}_{1111}^{(r)} &= \mathcal{A}_{2121}^{(r)} = G^{(r)} \lambda^2, \\ \mathcal{A}_{1212}^{(r)} &= G^{(r)} \left[ \frac{1}{\lambda^2} + \frac{B^2}{G^{(r)} \mu_0} + \frac{(m_s^{(r)} \mu_0)^2}{3\chi^{(r)} G^{(r)} \mu_0} - \frac{B}{m_s^{(r)} \mu_0} \coth \left( \frac{3\chi^{(r)} B}{m_s^{(r)} \mu_0} \right) \right], \end{aligned} \quad (\text{A.4})$$

$$\begin{aligned} \mathcal{A}_{2222}^{(r)} &= G^{(r)} \left[ \frac{1}{\lambda^2} + \frac{B^2}{G^{(r)} \mu_0} - \frac{(m_s^{(r)} \mu_0)^2}{3\chi^{(r)} G^{(r)} \mu_0} + \frac{3\chi^{(r)} B^2}{G^{(r)} \mu_0} \left( \text{csch} \left( \frac{3\chi^{(r)} B}{m_s^{(r)} \mu_0} \right) \right)^2 \right], \\ \mathcal{H}_{11}^{(r)} &= \frac{1}{\mu_0} \left[ 1 + \frac{(m_s^{(r)} \mu_0)^2}{3\chi^{(r)} B^2} - \chi^{(r)} \frac{m_s^{(r)} \mu_0}{B} \coth \left( \frac{3\chi^{(r)} B}{m_s^{(r)} \mu_0} \right) \right], \\ \mathcal{H}_{22}^{(r)} &= \frac{1}{\mu_0} \left[ 1 - \frac{(m_s^{(r)} \mu_0)^2}{3\chi^{(r)} B^2} + 3\chi^{(r)} \left( \text{csch} \left( \frac{3\chi^{(r)} B}{m_s^{(r)} \mu_0} \right) \right)^2 \right], \end{aligned} \quad (\text{A.5})$$

and

$$\begin{aligned} \mathcal{M}_{121}^{(r)} &= \mathcal{M}_{211}^{(r)} = \frac{B}{\mu_0} \left[ 1 + \frac{(m_s^{(r)} \mu_0)^2}{3\chi^{(r)} B^2} - \frac{m_s^{(r)} \mu_0}{B} \coth \left( \frac{3\chi^{(r)} B}{m_s^{(r)} \mu_0} \right) \right], \\ \mathcal{M}_{222}^{(r)} &= \frac{B}{\mu_0} \left[ 2 - \frac{(m_s^{(r)} \mu_0)^2}{3\chi^{(r)} B^2} + 3\chi^{(r)} \left( \text{csch} \left( \frac{3\chi^{(r)} B}{m_s^{(r)} \mu_0} \right) \right)^2 \right]. \end{aligned} \quad (\text{A.6})$$

## Appendix B. Components of matrix **R**

Here, we provide the non-zero components of matrix **R**, namely,

$$\begin{aligned}
 R_{12} &= 1, \\
 R_{31} &= R_{54} = -ik_1, \\
 R_{21} &= k_1^2 \beta (\mathcal{A}_{1111} \mathcal{H}_{11} + \mathcal{M}_{121}^2 - \mathcal{M}_{121} \mathcal{M}_{222}), \\
 R_{25} &= -ik_1 \beta \mathcal{H}_{22} \mathcal{M}_{121}, \\
 R_{26} &= ik_1 \beta \mathcal{H}_{11}, \\
 R_{41} &= -k_1^2 \beta [\mathcal{A}_{1111} \mathcal{M}_{121} + \mathcal{A}_{1212} (\mathcal{M}_{121} - \mathcal{M}_{222})], \\
 R_{45} &= ik_1 \beta \mathcal{A}_{1212} \mathcal{H}_{22}, \\
 R_{46} &= -ik_1 \beta \mathcal{M}_{121}, \\
 R_{62} &= -ik_1 \mathcal{A}_{2222}, \\
 R_{63} &= -k_1^2 \mathcal{A}_{2121}, \quad \text{and} \\
 R_{64} &= ik_1 (\mathcal{M}_{121} - \mathcal{M}_{222}),
 \end{aligned} \tag{B.1}$$

where  $\beta = (\mathcal{A}_{1212} \mathcal{H}_{11} - \mathcal{M}_{121}^2)^{-1}$ .

## References

- [1] Erb RM, Libanori R, Rothfuchs N, Studart AR. Composites reinforced in three dimensions by using low magnetic fields. *Science* 2012;335:199–204.
- [2] Ginder J, Clark S, Schlotter W, Nichols M. Magnetostrictive phenomena in magnetorheological elastomers. *Int J Mod Phys B* 2002;16:2412–8.
- [3] Ginder JM, Schlotter WF, Nichols ME. Magnetorheological elastomers in tunable vibration absorbers. *Smart structures and materials 2001: damping and isolation volume 4331*. International Society for Optics and Photonics; 2001. p. 103–10.
- [4] Wang Q, Dong X, Li L, Ou J. Mechanical modeling for magnetorheological elastomer isolators based on constitutive equations and electromagnetic analysis. *Smart Mater Struct* 2018;27:065017.
- [5] Gong X, Fan Y, Xuan S, Xu Y, Peng C. Control of the damping properties of magnetorheological elastomers by using polycaprolactone as a temperature-controlling component. *Ind Eng Chem Res* 2012;51:6395–403.
- [6] Yang J, Gong X, Deng H, Qin L, Xuan S. Investigation on the mechanism of damping behavior of magnetorheological elastomers. *Smart Mater Struct* 2012;21:125015.
- [7] Lanotte L, Ausanio G, Hison C, Iannotti V, Luopio C. The potentiality of composite elastic magnets as novel materials for sensors and actuators. *Sens Actuators, A* 2003;106:56–60.
- [8] Tian TF, Li WH, Deng YM. Sensing capabilities of graphite based mr elastomers. *Smart Mater Struct* 2011;20:025022.
- [9] Farshad M, Roux ML. A new active noise abatement barrier system. *Polym Test* 2004;23:855–60.
- [10] Mohammadi NK, Galich PI, Krushynska AO, Rudykh S. Soft magnetoactive laminates: large deformations, transverse elastic waves and band gaps tunability by a magnetic field. *J Appl Mech* 2019;86.
- [11] Ciambella J, Stanier DC, Rahatekar SS. Magnetic alignment of short carbon fibres in curing composites. *Compos Part B* 2017;109:129–37.
- [12] Kim Y, Yuk H, Zhao R, Chester SA, Zhao X. Printing ferromagnetic domains for untethered fast-transforming soft materials. *Nature* 2018;558:274–9.
- [13] Stanier DC, Ciambella J, Rahatekar SS. Fabrication and characterisation of short fibre reinforced elastomer composites for bending and twisting magnetic actuation. *Compos Part A* 2016;91:168–76.
- [14] Tang S-Y, Zhang X, Sun S, Yuan D, Zhao Q, Yan S, et al. Versatile microfluidic platforms enabled by novel magnetorheological elastomer microactuators. *Adv Funct Mater* 2018;28:1705484.
- [15] Makarova LA, Alekhina YA, Rusakova TS, Perov NS. Tunable properties of magnetoactive elastomers for biomedical applications. *Phys Procedia* 2016;82:38–45.
- [16] Hu W, Lum GZ, Mastrangeli M, Sitti M. Small-scale soft-bodied robot with multimodal locomotion. *Nature* 2018;554:81–5.
- [17] Yim S, Sitti M. Design and rolling locomotion of a magnetically actuated soft capsule endoscope. *IEEE Trans Rob* 2011;28:183–94.
- [18] Jolly MR, Carlson JD, Munoz BC. A model of the behaviour of magnetorheological materials. *Smart Mater Struct* 1996;5:607–14.
- [19] Bastola AK, Hossain M. A review on magneto-mechanical characterizations of magnetorheological elastomers. *Compos Part B* 2020;108348.
- [20] Danas K, Kankanala SV, Triantafyllidis N. Experiments and modeling of iron-particle-filled magnetorheological elastomers. *J Mech Phys Solids* 2012;60:120–38.
- [21] Abramchuk S, Grishin D, Kramarenko EY, Stepanov G, Khokhlov A. Effect of a homogeneous magnetic field on the mechanical behavior of soft magnetic elastomers under compression. *Polym Sci Ser A* 2006;48:138–45.
- [22] Soria-Hernández CG, Palacios-Pineda LM, Elías-Zúñiga A, Perales-Martínez IA, Martínez-Romero O. Investigation of the effect of carbonyl iron micro-particles on the mechanical and rheological properties of isotropic and anisotropic MREs: constitutive magneto-mechanical material model. *Polymers* 2019;11:1705.
- [23] Bednarek S. The giant magnetostriction in ferromagnetic composites within an elastomer matrix. *Appl Phys A* 1999;68:63–7.
- [24] Guan X, Dong X, Ou J. Magnetostrictive effect of magnetorheological elastomer. *J Magn Magn Mater* 2008;320:158–63.
- [25] Lanotte L, Ausanio G, Iannotti V, Luopio Jr C. Influence of particle pre-orientation on elastomagnetic effect in a composite material of ellipsoidal ni microparticles in a silicone matrix. *Appl Phys A* 2003;77:953–8.
- [26] Moreno M, Gonzalez-Rico J, Lopez-Donaire M, Arias A, Garcia-Gonzalez D. New experimental insights into magneto-mechanical rate dependences of magnetorheological elastomers. *Compos. Part B* 2021;224:109148.
- [27] Dargahi A, Sedaghati R, Rakheja S. On the properties of magnetorheological elastomers in shear mode: design, fabrication and characterization. *Compos Part B* 2019;159:269–83.
- [28] Brown WF. *Magnetoelastic interactions* vol. 9. Springer; 1966.
- [29] Maugin GA, Eringen AC. Deformable magnetically saturated media. i. field equations. *J Math Phys* 1972;13:143–55.
- [30] Tiersten H. Coupled magnetomechanical equations for magnetically saturated insulators. *J Math Phys* 1964;5:1298–318.
- [31] Toupin RA. The elastic dielectric. *Arch Ration Mech Anal* 1956;5:849–915.
- [32] Truesdell C, Toupin R. *The classical field theories*. Handbuch der Physik, vol. III. Springer, Berlin; 1960.
- [33] Dorfmann A, Ogden RW. Nonlinear magnetoelastic deformations. *Q J Mech Appl Math* 2004;57:599–622.
- [34] Kankanala SV, Triantafyllidis N. On finitely strained magnetorheological elastomers. *J Mech Phys Solids* 2004;52:2869–908.
- [35] Vu DK, Steinmann P. Nonlinear electro- and magneto-elastostatics: material and spatial settings. *Int J Solids Struct* 2007;44:7891–905.
- [36] Garcia-Gonzalez D, Hossain M. A microstructural-based approach to model magneto-viscoelastic materials at finite strains. *Int J Solids Struct* 2020;208:119–32.
- [37] Ivaneyko D, Toshchevikov V, Saphiannikova M, Heinrich G. Mechanical properties of magneto-sensitive elastomers: unification of the continuum-mechanics and microscopic theoretical approaches. *Soft Matter* 2014;10:2213–25.
- [38] Keip M-A, Rambausk M. Computational and analytical investigations of shape effects in the experimental characterization of magnetorheological elastomers. *Int J Solids Struct* 2017;121:1–20.
- [39] Javili A, Chatzigeorgiou G, Steinmann P. Computational homogenization in magneto-mechanics. *Int J Solids Struct* 2013;50:4197–216.
- [40] Keip M-A, Rambausk M. A multiscale approach to the computational characterization of magnetorheological elastomers. *Int J Numer Methods Eng* 2016;107:338–60.
- [41] Castañeda PP, Galipeau E. Homogenization-based constitutive models for magnetorheological elastomers at finite strain. *J Mech Phys Solids* 2011;59:194–215.
- [42] Galipeau E, Castañeda PP. The effect of particle shape and distribution on the macroscopic behavior of magnetoelastic composites. *Int J Solids Struct* 2012;49:1–17.
- [43] Galipeau E, Rudykh S, deBotton G, Castañeda PP. Magnetoactive elastomers with periodic and random microstructures. *Int J Solids Struct* 2014.
- [44] Rudykh S, Lewinstein A, Uner G, deBotton G. Analysis of microstructural induced enhancement of electromechanical coupling in soft dielectrics. *Appl Phys Lett* 2013;102:151905.
- [45] Tian L, Tevet-Deree L, deBotton G, Bhattacharya K. Dielectric elastomer composites. *J Mech Phys Solids* 2012;60:181–98.
- [46] Goshkoderia A, Arora N, Slesarenko V, Li J, Chen V, Juhl A, et al. Tunable permittivity in dielectric elastomer composites under finite strains: periodicity, randomness, and instabilities. *Int J Mech Sci* 2020;186:105880.

- [47] Arora N, Li J, Slesarenko V, Rudykh S. Microscopic and long-wave instabilities in 3D fiber composites with non-gaussian hyperelastic phases. *Int J Eng Sci* 2020;157: 103408.
- [48] Geymonat G, Müller S, Triantafyllidis N. Homogenization of nonlinearly elastic materials, microscopic bifurcation and macroscopic loss of rank-one convexity. *Arch Ration Mech Anal* 1993;122:231–90.
- [49] Greco F, Leonetti L, Lonetti P, Luciano R, Pranno A. A multiscale analysis of instability-induced failure mechanisms in fiber-reinforced composite structures via alternative modeling approaches. *Compos Struct* 2020;112529.
- [50] Li J, Arora N, Rudykh S. Elastic instabilities, microstructure transformations, and pattern formations in soft materials. *Curr Opin Solid State Mater Sci* 2021;25: 100898.
- [51] Li J, Pallicity TD, Slesarenko V, Goshkoderia A, Rudykh S. Domain formations and pattern transitions via instabilities in soft heterogeneous materials. *Adv Mater* 2019;31:1807309.
- [52] Rosen BW. Mechanics of composite strengthening. *Fibre composite materials American society of metals, Ohio*. 2020. p. 37–75.
- [53] Rudykh S, deBotton G. Instabilities of hyperelastic fiber composites: micromechanical versus numerical analyses. *J Elast* 2012;106:123–47.
- [54] Arora N, Batan A, Li J, Slesarenko V, Rudykh S. On the influence of inhomogeneous interphase layers on instabilities in hyperelastic composites. *Materials* 2019;12: 763.
- [55] Slesarenko V, Rudykh S. Microscopic and macroscopic instabilities in hyperelastic fiber composites. *J Mech Phys Solids* 2017;99:471–82.
- [56] Triantafyllidis N, Maker BN. On the comparison between microscopic and macroscopic instability mechanisms in a class of fiber-reinforced composites. *J Appl Mech* 1985;52:794–800.
- [57] Florijn B, Coulaïs C, van Hecke M. Programmable mechanical metamaterials: the role of geometry. *Soft Matter* 2016;12:8736–43.
- [58] Kochmann DM, Bertoldi K. Exploiting microstructural instabilities in solids and structures: from metamaterials to structural transitions. *Appl Mech Rev* 2017;69: 050801.
- [59] Bertoldi K, Boyce MC. Mechanically triggered transformations of phononic band gaps in periodic elastomeric structures. *Phys Rev B* 2008;77:052105.
- [60] Rudykh S, Boyce M. Transforming wave propagation in layered media via instability-induced interfacial wrinkling. *Phys Rev Lett* 2014;112:034301.
- [61] Li J, Slesarenko V, Rudykh S. Auxetic multiphase soft composite material design through instabilities with application for acoustic metamaterials. *Soft Matter* 2018; 14:6171–80.
- [62] Shim J, Shan S, Košmrlj A, Kang SH, Chen ER, Weaver JC, Bertoldi K. Harnessing instabilities for design of soft reconfigurable auxetic/chiral materials. *Soft Matter* 2013;9:8198–202.
- [63] Li J, Rudykh S. Tunable microstructure transformations and auxetic behavior in 3D-printed multiphase composites: the role of inclusion distribution. *Compos Part B* 2019;172:352–62.
- [64] Krishnan D, Johnson H. Optical properties of two-dimensional polymer photonic crystals after deformation-induced pattern transformations. *J Mech Phys Solids* 2009;57:1500–13.
- [65] Ottenio M, Destrade M, Ogden R. Incremental magnetoelastic deformations, with application to surface instability. *J Elast* 2008;90:19–42.
- [66] Kankanala SV, Triantafyllidis N. Magnetoelastic buckling of a rectangular block in plane strain. *J Mech Phys Solids* 2008;56:1147–69.
- [67] Rudykh S, Bertoldi K. Stability of anisotropic magnetorheological elastomers in finite deformations: a micromechanical approach. *J Mech Phys Solids* 2013;61: 949–67.
- [68] Danas K, Triantafyllidis N. Instability of a magnetoelastic layer resting on a non-magnetic substrate. *J Mech Phys Solids* 2014;69:67–83.
- [69] Goshkoderia A, Rudykh S. Stability of magnetoactive composites with periodic microstructures undergoing finite strains in the presence of a magnetic field. *Composites Part B* 2017;128:19–29.
- [70] Goshkoderia A, Chen V, Li J, Juhl A, Buskohl P, Rudykh S. Instability-induced pattern formations in soft magnetoactive composites. *Phys Rev Lett* 2020;124: 158002.
- [71] Psarra E, Bodelot L, Danas K. Two-field surface pattern control via marginally stable magnetorheological elastomers. *Soft Matter* 2017;13:6576–84.
- [72] Coleman BD, Noll W. The thermodynamics of elastic materials with heat conduction and viscosity. *The foundations of mechanics and thermodynamics*. Springer; 1974. p. 145–56.
- [73] Kovetz A. *Electromagnetic theory* vol. 975. Oxford University Press Oxford; 2000.
- [74] Wu B, Destrade M. Wrinkling of soft magneto-active plates. *Int J Solids Struct* 2021;208:13–30.
- [75] Dorfmann A, Haughton D. Stability and bifurcation of compressed elastic cylindrical tubes. *Int J Eng Sci* 2006;44:1353–65.
- [76] Slesarenko V, Rudykh S. Harnessing viscoelasticity and instabilities for tuning wavy patterns in soft layered composites. *Soft Matter* 2016;12:3677–82.